SELECTIVE HEATING OF VASCULAR STRUCTURES TO CREATE CONTRAST IN MEDICAL MID-IR IMAGES

by

Jason Randolph Case

A dissertation submitted to the faculty of
The University of North Carolina at Charlotte
in partial fulfillment of the requirements
for the degree of Doctor of Philosophy in
Optical Science and Engineering

Charlotte

2015

Approved by:

_____
Dr. Susan Trammell

_____
Dr. Glenn Boreman

_____
Dr. Nathaniel Fried

_____
Dr. Yasin Raja

_____
Dr. Didier Dreau

_____
Dr. Russell Keanini

ABSTRACT

JASON RANDOLPH CASE. Selective heating of vascular structures to create contrast in medical Mid-IR images (DR. SUSAN R. TRAMMELL)

The goal of this study is to develop an enhanced mid-IR imaging modality for mapping vascular structures. This imaging technique is intended for real-time use by medical professionals during surgical procedures such as tumor removal and vascular malformation correction. This novel enhanced thermal imaging method is a combination of IR imaging (8-10 μm) and selective heating of blood (~0.5 °C) relative to surrounding water-rich tissue using LED sources at low powers. The selective heating provides contrast in the mid-IR images. Post-acquisition processing of these images highlights temporal and spatial changes revealing vascular structures.

Initial studies were completed to determine which type of light source was most effective for preferentially heating hemoglobin and thus creating thermal contrast in mid-IR images. *Ex vivo* tissue samples (porcine blood, skeletal muscle, skin and fat) were illuminated with LEDs that emit at 405 nm and 530 nm (closely matching the wavelengths of blood absorption peaks). Illumination with the 530 nm LED at low powers (irradiance <500 mW/cm^2) was more effective at selectively heating blood relative to other tissue types compared to the 405 nm LED.

Experiments were conducted to test the ability of our method to map the existing supportive vasculature in porcine heart tissue *ex vivo*. Blood was injected into a vessel and heated with the LED. We developed an image processing method that highlights temporal and spatial variations in temperature that allowed the mapping of vessels as

deep as 0.75 cm below the tissue surface and up to 16 cm from the location of the LED spot. These studies demonstrate that enhanced thermal imaging is a promising imaging modality for medical applications in which determining the location and morphology of vasculature is important.

COMSOL Multiphysics, finite element analysis software package, was used to create models of heated vessels embedded in muscle tissue to help develop an algorithm to determine the depth and size of vessels based on the two dimensional thermal images. Gelatin based tissue phantoms were used to verify the algorithm's ability to determine depth and size of heated resistive wires embedded within them. We also used surface temperature profiles and thermal signal arrival time; we were successful at predicting depths and sizes for vessels embedded deeper than 2 mm in muscle tissue.

The enhanced thermal imaging technique was used for tumor margin detection *in vivo*. Fluorescent, enhanced thermal and standard imaging modalities as well as physical caliper measurements were used to estimate breast cancer tumor volumes as a function of time in 19 mice over a 30-day study period. A strong correlation was (R^2 >0.9) found between tumor volumes estimated using fluorescent imaging, standard thermal imaging, caliper measurements and enhanced IR images, indicating that enhanced thermal imaging does monitor tumor growth. Further, the enhanced IR images showed a corona of bright emission along the edges of the tumor masses. Histology revealed that the bright corona is associated with the tumor margin. This novel mid-IR imaging technique could be used to estimate tumor margins in real-time during surgical procedures.

DEDICATION

To my wife Stacy who has supported me for the last seven and a half years with an unbelievable resolve. I doubt I will ever be able to repay you but I will spend the rest of my days trying.

ACKNOWLEDGMENTS

First, I would like to thank Dr. Susan Trammell. Without her help and influence this research would have not been possible. Dr. Trammell has been integral in my entire academic career from being my undergraduate advisor to now my thesis advisor on this dissertation.

Secondly, I would like to thank Dr. Glenn Boreman, Dr. Yasin Raja, Dr. Nathaniel Fried, Dr. Didier Dreau and Dr. Russell Keanini for taking the time to serve on my dissertation committee and supporting me through this challenging process. Their expertise has been an invaluable resource throughout my studies at the University of North Carolina at Charlotte.

In addition, I wish to thank Dr. Donald Jacobs and Dr. Pedram Leilabady, the two instructors who influenced me the most in my physics education. Dr. Leilabady is the person who convinced me to pursue an academic career in physics and optics. If not for him I would have never even attempted to get this far. Dr. Jacob's lectures taught me the logical thought processes that made me the scientist I am today. His abilities to capture a student's mind and guide them through the more difficult concepts in this field are amazing.

Also, I would like to thank my fellow graduate students Madison Young and Aubrey Shipley whose assistance with data collection made completing the tests much more feasible and effective.

Finally I would like to thank my family and friends for their support and compromise that has allowed me to achieve my goals.

TABLE OF CONTENTS

CHAPTER 1: INTRODUCTION

1.1 Motivation

The goal of this study is to develop an enhanced mid-IR imaging modality for mapping vascular structures. This imaging technique is intended for real-time use by medical professionals during surgical procedures that require vascular manipulation such as aneurysm repair, tumor removal, and vascular malformation correction. This novel enhanced thermal imaging method is a combination of IR imaging (8-10 μm) and selective heating of blood (~0.5 °C) relative to surrounding water-rich tissue using LED sources at low powers. The selective heating provides contrast in the mid-IR images and post-acquisition processing of these images highlights temporal and spatial changes in temperature that are sensitive to the presence of blood vessels.

This innovative imaging technique takes advantage of recent advances in thermal imaging camera technology and LED light sources. Many biomedical imaging techniques involve the use of X-rays, which are a type ionizing radiation and can damage biological tissues. Further, X-ray imaging often involves the use of contrast agents that can cause allergic reactions in some patients. Enhanced thermal imaging does not use ionizing radiation, does not damage tissue and does not require the use of dyes or other chemical contrast agents.

1.2 Blackbody Radiators

In thermal imaging the human body is treated as a blackbody radiator. The total energy radiated per unit of surface area of a blackbody (F) is described by the Stefan-Boltzmann Law,

$$F = \sigma T^4$$

Where σ is the Stefan-Boltzmann constant and T is the temperature of the object in Kelvins. As a blackbody experiences an increase in temperature, it exhibits an increase in irradiance (becomes brighter, Figure 1.1). Wien's law describes the wavelength at which a blackbody emits the most energy (λ_{max}),

$$\lambda_{max} = \frac{b}{T}$$

Where T is the temperature of the blackbody in K and b is a constant. At normal body temperatures human subjects have a peak emission at 9.5 µm.

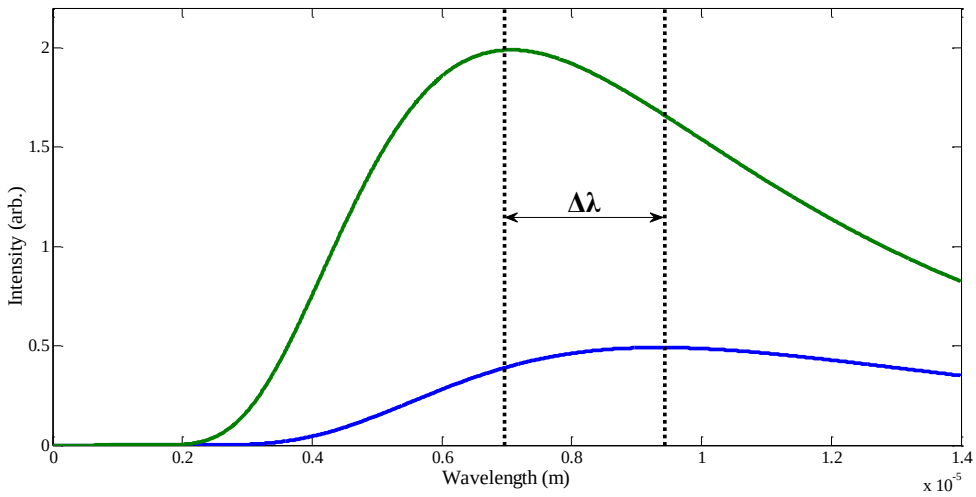

Figure 1.1: Blackbody curves for objects at two different temperatures. These curves show objects whose temperatures differ by 100 °K. The blue line is at 310 °K while the upper green plot line is at 410 °K. Notice the warmer blackbody is brighter at all wavelengths.

Thermal imaging assumes that the human body acts as a nearly perfect blackbody radiator at mid-IR wavelengths. Emissivity (ε) is the fractional amount of light that is emitted by an object and the reflectance, R, is the amount of light (from other light sources) that is reflected by an object. A perfect blackbody radiator has an emissivity of 1, which means all light coming from the source is produced by the source and there is no light reflected by the source. The emissivity of the human body is approximately one in the mid-IR. (See Table 1.1)[1]

Table 1.1: Emissivity of human tissues as 40°C at infrared wavelengths[1]

Tissue	**Emissivity**
Dark Skin (3-12 μm)	0.98 ±0.01
White Skin (3-12 μm)	0.97 ±0.02
Burnt Skin (3-12 μm)	0.97 ±0.02
Pericardium (9 μm)	0.95

1.3 Thermal (Mid-IR) Cameras

IR detectors are called bolometers or calorimeters. Bolometers are designed to measure a change in resistance that is related to a change in temperature. The change in temperature is proportional to the amount of energy absorbed by the thermal mass of the bolometer. These devices consist of a material of known heat capacity connected to a thermal reservoir by a resistor whose performance under varying temperature is well understood. A voltage is applied to the circuit containing the resistive element material. When the heat absorbing material is exposed to incident radiation a change in temperature is created in the bolometer circuit. The temperature change in the circuit

alters its effective resistance. This resistance change follows the Steinhart-Hart equation for nonlinear temperature dependent resistance.

$$\frac{1}{T} = A + B \ln R + C \ln R^3$$

For this equation T is temperature in Kelvin and R is the measured resistance in Ohms of the thermistor at T. A, B and C are the Steinhart-Hart coefficients which are a device property depending on the thermistor used. Figure 1.2 shows a layout of a single simple bolometer. The IR camera (SC600 series) (FLIR Systems©, Boston, MA USA) used for this study has a 640 x 480 array of microbolometers.

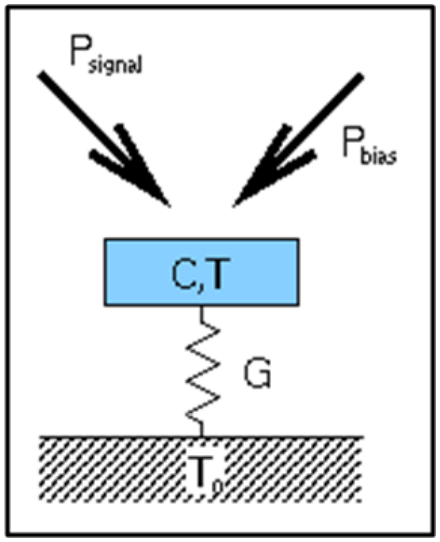

Figure1.2: Simple depiction of a bolometer. Power (P_{signal}) from an incident signal is absorbed by the bolometer and heats up a thermal mass with heat capacity (C) and temperature (T) and initial Power Bias (P_{bias}). The thermal mass is connected to a constant temperature (T_0) reservoir through a linkage of thermal conductance G. Temperature changes as $\Delta T = (P_{signal}+P_{Bias})/G$. This change is measured with a resistive thermometer (thermistor).[2]

1.4 Standard Thermal Imaging

Thermography, as a tool for medical diagnosis, was first introduced into medicine in the 1960's.[3] Since that time thermal imaging has been used for the diagnosis and study of diabetic neuropathy[4,5–11], the evaluation and treatment of burns[12], the evaluation of superficial vascular disorders[13–16], breast cancer detection[4,17–22] along with many other applications (see Lahiri et al. for a recent review[1]). In addition, evaluating surface temperatures of animals has become common place in veterinary medicine. Thermal images have been used to evaluate lameness is horses by detecting regions of inflammation and other irregularities.[23] Thermal imaging has also been used to detect rabies in wild raccons by monitoring the temperature of the nose.[24]

In all standard applications thermography is used to find areas of tissue that have an increase or decrease in temperature, which results from an increase or decrease in blood flow. Standard thermography only shows differences in tissue temperatures and does not reveal the detailed structures of tissues or differentiate between types of tissue. Further, this technique is often heavily dependent on the accurate determination of thermal background and/or careful control of the surrounding environment during imaging. These issues have limited the utility of thermal imaging in medicine.

1.5 Novel Enhanced Thermal Imaging

Enhanced thermal imaging combines the concepts of thermography and selective heating to highlight vascular structures in thermal images. This combination of techniques allows enhanced thermal imaging to specifically target a tissue type, blood vessels, for imaging. Further, this technique is not sensitive to environmental and

background temperature changes. Recall that the brightness of a blackbody radiator increases dramatically as the temperature of the object increases.

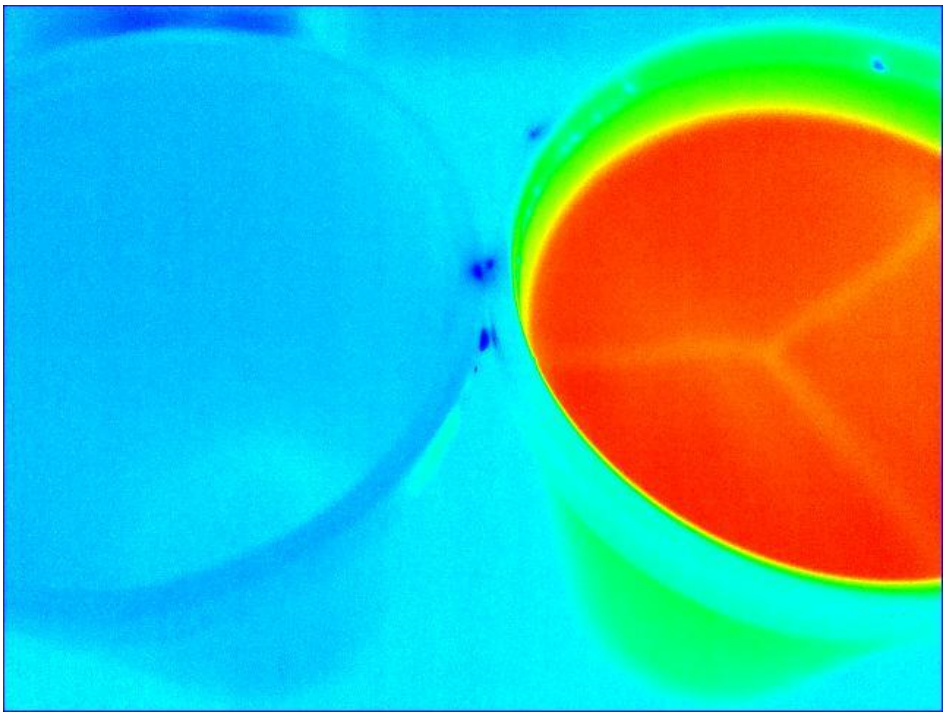

Figure 1.3: Thermal Contrast Example. This image compares a room temperature cup of coffee (left) and a warm cup of coffee (right). Notice that regions of different temperature are easily seen in the image of the warm cup but few details can be seen in the room temperature cup as it is in thermal equilibrium with the environment. This image was acquired with a FLIR thermal IR camera by the author.

Enhanced thermal imaging uses LED light sources to selectively heat blood/blood vessels (by about 0.5 °C) with respect to surrounding water-rich soft tissue. The warm blood/blood vessels appear brighter than surrounding tissue in a thermal image. The amount of heating (< 1 °C) is well below levels considered dangerous to biological systems.[25] Figure 1.3 shows an example of thermal contrast in a mid-IR image. The cup containing warmer coffee appears much brighter in the image. Our enhanced mid-IR imaging technique creates a similar contrast between blood and surrounding tissue.

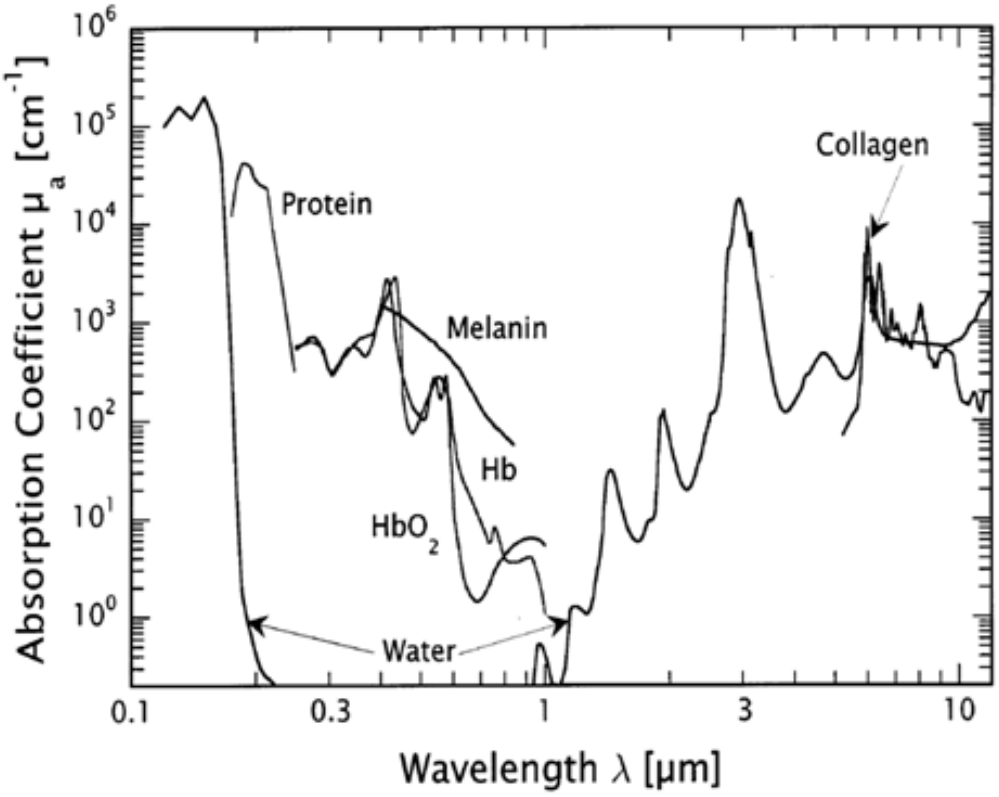

Figure 1.4: Hemoglobin absorption curves showing the absorption peaks for oxygenated and de-oxygenated hemoglobin, protein, collagen, melanin and water. Notice the hemoglobin peaks around 420 and 530 nm. These peaks lie inside a minimum for water absorption.[26]

Hemoglobin absorbs light strongly at 420 nm and 530 nm (See Figure 1.4).[26] These absorption peaks lie inside the minimum for absorption by water (a major component of soft tissues). When tissue is irradiated with light of wavelength near 420 nm and 530 nm, blood will absorb much of this energy and will heat more than soft tissue. Selective heating of blood is used in laser treatments of vascular lesions such as port wine stain.[27] A laser with wavelength of 585 nm to 595 nm heats and coagulates blood vessels, while leaving surrounding water-rich tissue undamaged. We are applying a similar methodology to selectively heat blood (without coagulating the blood or

damaging the water-rich tissue) to provide a contrast agent for enhanced thermal imaging.

A temperature contrast can be created by cooling a region of tissue and then allowing warm blood to flow back into the region. This method has the drawback that cooling can reduce blood flow and constrict blood vessels. Small vessels would not be accurately mapped using this type of technique.

1.6 Current Medical Imaging Techniques

Imaging modalities widely used in medicine today include Magnetic Resonance Imaging (MRI), Computed Tomography (CT) scanning and ultrasound. CT and MRI provide excellent spatial resolution, but cannot be used in real time during surgical procedures. Ultrasound can be used during procedures, but does not provide adequate spatial resolution or the ability to discern detailed structure in tissues, such as tumor margins.

MRI is useful for tissues with many hydrogen nuclei and low density (soft, water-rich tissues) like brain, muscle, connective tissue and most tumors. MRI scanners generate a strong magnetic field that aligns the protons in soft tissue to the direction of the field. A radio frequency (RF) signal is broadcast into the body and the protons absorb a small amount of this energy, which flips the spins of the protons into an excited energy state. When the external RF signal is turned off, the proton spins become re-aligned with the static magnetic field. During this relaxation, an RF signal is generated by the protons and this signal is collected and assembled into a 3-D image of the patient. The protons in different tissues reach spin equilibrium at different rates and this provides contrast between different types of tissue. In addition, contrast agents can be used to alter the

relaxation times of atoms within tissues to enhance the appearance of structures such as blood vessels, tumors and inflammation.[28] MRI images have good spatial resolution (~0.2 mm) and are capable of imaging many different tissue types. However, the use of MRI is limited in real-time during procedures due to the slow imaging speed, the size of the equipment and the strong magnetic fields created by the scanner.[29]

CT is another common method for imaging internal structures, including blood vessels. CT scans capture a series of x-rays taken from multiple angles and these scans are then assembled into a 3-D rendering of the target. Advanced CT scanners use a helical scanning path to continuously collect images and reduce imaging times. CT scans have extremely high spatial resolution (~0.1-0.2 mm) and excellent penetration depth. X-ray contrast agents are used for imaging soft tissues and these dyes can cause allergic reactions and other complications in some patients.[30] Further, CT scanning uses x-rays, a form of ionizing radiation, which can be harmful to living tissue. Using CT scans in a real-time environment is not possible due to the size of the equipment and slow scanning speeds.[31]

Standard ultrasound is a common imaging modality that uses sound waves to probe structures in tissue. Sounds waves are sent into tissue and the back-reflected waves are measured with a probe in contact with the patient. A more advanced version of ultrasound uses the Doppler Effect to measure blood flow. The spatial resolution of ultrasound is poor (~ 0.5 mm) when compared to other available techniques. Further, the ultrasound's probe must remain in contact with the tissue's surface during imaging which limits its use during surgical procedures when a continuous real-time imaging modality is required.[32]

Optical coherence tomography (OCT) is a noninvasive, high spatial resolution imaging method (0.01-0.03mm). In OCT, light is used to collect information about the subject. One form of OCT uses a Michelson interferometer to image the subject. A broadband near-IR source is split into two beams; the first is focused on the subject and the other is used as a reference beam. The subject beam scans the surface of the object being studied. When this beam is reflected off the subject it is sent to the interferometer where it is combined with the reference beam. The resulting interference pattern is analyzed to form an image with excellent spatial resolution (10-30 μm). OCT has an imaging depth limited to 1.0 - 2.0 mm due to the large scattering of optical light in tissue. While OCT does produce real-time images, the field of view is limited and the technique requires scanning to acquire an image.[33]

Optoacoustic, or photoacoustic, imaging uses a series of optical pulses to produce a temperature change in tissue through light absorption. Rapid expansion and contraction in the tissue, caused by the temperature change, produces an acoustic wave. This sound wave is then captured in the same way as the back reflected wave in ultrasound techniques.[34] Images created using this technique have a high spatial resolution, but the probe must be in contact with the patient and the technique requires scanning to acquire an image. Also an expensive short-pulsed laser source is required for this technique. Photoacoustic imaging is still under investigation and has not seen wide use in medical settings currently but has seen success in the field, such as its use imaging tumor ablation in studies performed by Laufer et al.[35]

Enhanced thermal imaging uses external illumination to selectively heat blood to create contrast in mid-IR images. Enhanced mid-IR imaging shares similarities with

standard thermal imaging (See Section 1.4) however; the method we have developed overcomes one of the main limitations of standard thermal techniques – the inability to differentiate between tissue types. Enhanced thermal imaging can operate in real-time without being in contact with the imaging area making this an attractive option for use during surgical procedures. Enhanced mid-IR imaging does not use ionizing radiation or injectable contrast agents. The current system uses readily available, off-the-shelf components making it an affordable option for both hospital and clinic use. Currently our system has a maximum spatial resolution of 0.26 mm which is lower than MRI and CT but better than that of standard low frequency ultrasound. The spatial resolution of our system can be further enhanced with the addition of different lenses and the use of different mid-IR detector arrays. Table 2 compares our enhanced thermal imaging technique with other commonly used medical imaging modalities.

Table 2**:** Comparison of imaging techniques.[36,11,12,37]

Method	Advantages	Disadvantages
Ultrasound	· Noninvasive · Images are real-time · Equipment is cost effective	· Low quality images · Requires trained technician to interpret images · Probe must be in contact with patient and this limits use during some surgical procedures
Magnetic Resonance Imaging (MRI)	· Good spatial resolution (1-mm) · Minimally invasive (except for intravenous contrast agents) · Produces 3D image · Penetrates all tissue types	· Image creation is time consuming (not real-time) · Patients may be allergic to contrast agents · Blood flow cannot be imaged (Blood flows at a much faster rate than the MRI can scan) · Equipment is very expensive and large · Strong magnetic field prevents the use of MRI in surgical procedures
Computed Tomography (CT)	· Good quality images and spatial resolution (500 µm) · Penetrates all soft tissue types soft tissue (only limited in imaging through more dense tissue such as bone) · Minimally invasive (except for intravenous contrast agents)	· Image creation is time consuming (not real-time) · Patients may be allergic to contrast agents · Blood flow cannot be imaged (Blood flows at a much faster rate than the CT scan can image) · Equipment is very large and costly · Uses X-rays (can damage tissue) · Equipment and methods limit use in surgical procedures
Optical Coherence Tomography (OCT)	· Good quality images · Equipment is small and cost is reasonable · Non invasive · Real-time images	· Small penetration depth (1-2 mm) · Method requires device to be near subject which limits procedures that require more open access to the surgical area · Scanning is required to acquire image
Photoacoustic Imaging	· Good quality images · Uses widely available components (ultrasound probes, lasers, etc.) · Non invasive	· Low penetration depth (similar to OCT scans) · Not fully developed for medical use (still under investigation) · Scanning is required to acquire image
Standard Thermal Imaging	· Real-time images · No scanning required · No ionizing radiation · No contrast agents needed	· Unable to target specific tissue types or differentiate between tissue types.
Enhanced Thermal Imaging (our technique)	· Resolution of 0.3 mm (can be improved with different optics) · Real-time images · No scanning required · No ionizing radiation · No contrast agents needed	· Only differentiates between blood/vessels and surrounding tissue; not selective for other tissue types.

1.7 This Study

In this study, we explore the viability of using LED sources to create a thermal contrast that can be used to map vascular structures (See Chapter 2). Initial studies were completed to determine which type of light source was most effective for preferentially heating hemoglobin, and thus blood and blood vessels, to create contrast in mid-IR images. *Ex vivo* tissue samples (porcine blood, skeletal muscle, skin and fat) were illuminated with LEDs that emit at 405 nm and 530 nm (matching the wavelengths of blood absorption peaks). Heating during LED irradiation as a function of time was measured using a thermal camera. Illumination of blood with the 530 nm LED at low powers (irradiance <500 mW/cm^2) was more effective at selectively heating blood (ΔT = 2-5°C) relative to other tissue types as compared to the 405 nm LED.

Experiments were then conducted to test our system's ability to map the existing supportive vasculature in porcine heart tissue *ex vivo* (See Chapter 3). Blood was injected into an existing vessel and heated with the LED. The path of the heated blood was mapped with the thermal camera. We developed an image processing method that highlights temporal and spatial variations in temperature that allowed the mapping of vessels as deep as 0.75 cm below the tissue surface and up to 16 cm from the location of the LED spot. These studies demonstrate that enhanced thermal imaging is a promising imaging modality for medical applications in which determining the location and morphology of vasculature is important.

COMSOL Multiphysics models of heated vessels embedded in muscle tissue were developed to create an algorithm to determine the depth and size of vessels based on the two dimensional thermal images (See Chapter 4). The algorithm uses surface temperature profiles and thermal signal arrival times to estimate depth and size of embedded vessels.

We applied this algorithm to our images of porcine heart tissue and were able to estimate the depths and sizes of these structures.

The enhanced thermal imaging technique was then used to determine tumor margins in a murine model (See Chapter 5). In this study, fluorescent, enhanced mid-IR and standard thermal imaging modalities as well as physical caliper measurements were used to estimate breast cancer tumor volumes as a function of time in 19 mice over a 30-day study period. Tumor volumes calculated from fluorescent imaging follow an exponential growth curve for the first 22 days of the study. Local necrosis affected the tumor volume estimates based on the fluorescent images after Day 22. The tumor volumes estimated from enhanced thermal imaging, standard thermal imaging and caliper measurements all show exponential growth over the entire study period. A strong correlation was found between tumor volumes estimated using fluorescent imaging, standard thermal imaging, caliper measurements with enhanced IR images, indicating that enhanced thermal imaging is capable of monitoring tumor growth. Further, the enhanced IR images revealed a corona of bright emission along the edges of the tumor masses. Histology revealed that the bright corona is associated with the tumor margin. This novel mid-IR imaging technique could be used to estimate tumor margins in real-time during surgical procedures.

CHAPTER 2: PRELIMINARY STUDIES: USING LED SOURCES TO SELECTIVELY HEAT BLOOD RELATIVE TO SURROUNDING WATER RICH TISSUE

2.1 Introduction

In this study, we present experimental results that demonstrate the ability of light-emitting diodes (LEDs) to selectivity heat blood relative to water-rich tissue. The selective heating can provide contrast in mid-IR images in order to map vascular structures. *Ex vivo* tissue samples (porcine blood, skeletal muscle, skin and fat) were illuminated with LEDs that emit at 405 nm and 530 nm (closely matching the wavelengths of blood absorption peaks). Heating during LED irradiation as a function of time was measured using a thermal camera. Illumination of blood with the 530 nm LED at low powers (irradiance <500 mW/cm^2) was more effective at selectively heating blood (ΔT = 2-5°C) relative to other tissue types as compared to the 405 nm LED. These studies demonstrate that selective heating combined with thermal imaging is a promising imaging modality for medical applications in which determining the location and morphology of vasculature is important.

2.2 Methods

A mid-IR camera (SC600 series) (FLIR Systems©, Boston, MA USA), sensitive from 7.5 to 14.0 microns, was used to record the heating response of porcine tissue samples that were illuminated with LED sources with wavelengths of 405 nm and 530

nm (close to blood absorption peaks). The camera has an array size of 640 x 480 pixels and a maximum frame rate of 200 fps. The LED sources have peak wavelengths of 405 nm (Thorlabs M405L2) and 530 nm (Thorlabs M530L2). The LED output was collimated using an aspheric collimation optic producing a 5 mm-diameter spot on the tissue surface. The 405 nm and 530 nm LED sources had maximum power outputs of 1500 and 1000 mW and spectral widths of 12 nm and 16 nm, respectively. Porcine tissue samples (skin, fat and skeletal muscle) and porcine blood were obtained from Animal Technologies, Inc. (Tyler, Texas). The blood was collected from donors sacrificed on the day of shipment and contained EDTA anticoagulant to prevent clotting. The tissue samples were kept hydrated and heated to body temperature (37 °C) using a saline bath and Peltier dish to maintain a constant temperature during all experiments.

The heating response to LED illumination for each tissue type was measured. The temperature of the tissue was monitored with the thermal camera as the tissue was continuously illuminated with the LED. Monitoring began 5 seconds before LED illumination to provide an initial measurement of the temperature of the tissue. The LED then illuminated the tissue surface for 60 seconds and imaging continued for 60 seconds after the LED was turned off to monitor the cooling of the tissue sample. We tested each tissue type with both the 405 nm and 530 nm LEDs at multiple LED output powers. Five data sets were collected for each LED power/tissue combination. The experimental setup is shown in Figure 2.1 and the LED parameters are summarized in Table 2.1.

Table 2.1: LED parameters for ex-vivo tissue experiments

Wavelength (nm):	405	530
Tissues types tested:	Blood, fat, skeletal muscle, skin	Blood, fat, skeletal muscle, skin
Spot Diameter (mm):	5	5
LED spectral width (nm):	12	16
Duration of LED exposure (s):	60	60

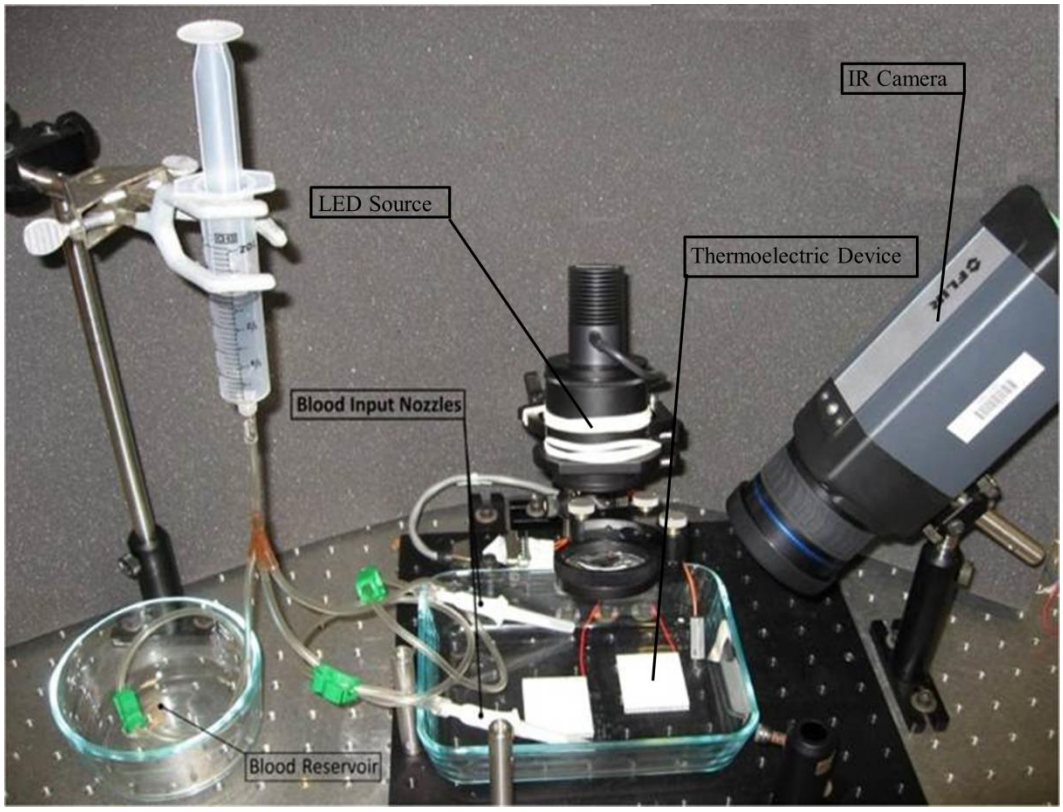

Figure 2.1: The experimental setup used for testing the heating response of porcine tissue and blood samples to LED illumination.

2.3 Results

Heating curves (ΔT versus time plots) were determined for all tissue types and LED irradiances used in the study. The average temperature of the tissue in the LED spot was measured in all frames of the recorded video during LED illumination. The average temperature of the same spot on the tissue was measured both before and after LED illumination to monitor the initial temperature and cooling of the tissue. The change in temperature, ΔT, as a function of time was determined by subtracting the initial temperature from the average temperature of the LED spot during heating and cooling. Figure 2 shows a representative heating curve (irradiance 473 mW/cm^2). Results for higher and lower LED irradiances show the same trends seen in Figure 2.2. Table 2.2 provides a summary of the maximum temperature rise for each tissue type for all LED irradiances. The standard deviation from the mean ΔT for all experiments was ~ 0.5 °C. The heating curves for the *ex vivo* tissue tests reveal that the greater the incident LED power, the greater the change in the temperature of all tissue types for both the 405 nm and 530 nm LEDs, as expected.

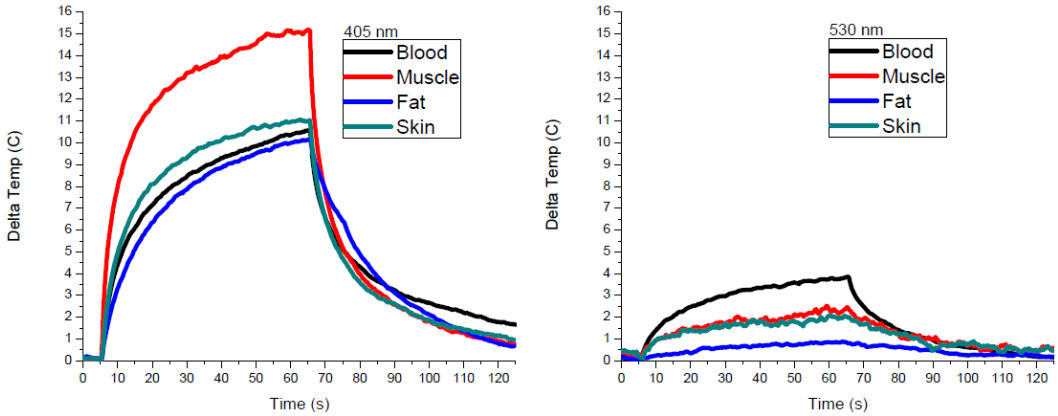

Fig 2.2: Temperature versus time plots for all porcine tissue types tested with irradiance 473 mW/cm^2. Panel A shows tissue heating in response to the 405 nm LED and Panel B shows tissue heating in response to the 530 nm LED. The blood heats more than the other tissue types upon illumination with the 530 nm LED indicating that this LED will be effective at selectively heating blood compared to surrounding tissue.

Table 2.2: Summary of results for tissue heating with 405 nm and 530 nm LEDs after 60 s of illumination. Note that due to output limitations for the 530 nm LED the maximum power density tested was slightly less than the 405 nm LED at 680 mW/cm^2.

	Blood	Fat	Skin	Muscle
Maximum ΔT achieved with 405 LED nm at 236 mW/cm^2 (°C)	5.7	5.0	6.0	7.0
Maximum ΔT achieved with 530 nm LED at 236 mW/cm^2 (°C)	1.2	≈0.0	1.1	1.2
Maximum ΔT achieved with 405 LED nm at 473 mW/cm^2 (°C)	10.5	10	11	15
Maximum ΔT achieved with 530 nm LED at 473 mW/cm^2 (°C)	4	<1	2.1	2.5
Maximum ΔT achieved with 405 LED nm at 708 mW/cm^2 (°C)	17	15.5	15.1	27
Maximum ΔT achieved with 530 nm LED at 680 mW/cm^2 (°C)	6.0	1.2	2.5	3.7

Illumination of blood with the 530 nm LED at low powers selectively heats blood with weak absorption by other tissue types. These results agree with our expectations based on the absorption coefficients and the well-studied behavior of tissue heating upon illumination with laser radiation at this wavelength.[26]

Tests with the 405 nm LED resulted in greater heating than was seen with the 530 nm LED (at the same output power) for all tissue types. The absorption coefficient for blood is larger than other tissue types near 405 nm and more than 10 times larger than the absorption coefficient for blood near 530 nm. This suggests that the 405 nm LED should be a more effective light source for selectively heating blood relative to other tissue types at low incident powers. However, the 405 nm LED tests showed that blood, skin and fat experienced comparable heating. This could be due to uncertainties or variability in absorption coefficients for different tissue types at this wavelength. Further, the skeletal muscle sample used in this study heated more than all other tissue types used in this study when illuminated with the 405 nm LED. Testing of additional muscle samples revealed that the heating for muscle was highly variable from sample to sample. An important difference between the muscle samples studied was the myoglobin content of the muscle tissue. Tissue samples with higher myoglobin content (selected by the redness of the tissue) heated more than samples with lower myoglobin content.

2.4 Discussion

LEDs were used to selectivity heat blood relative to surrounding water-rich tissue and this selective heating can likely be used to provide contrast in mid-IR images to reveal the morphology of vascular structures. Illumination of blood with the 530 nm LED

at low powers (irradiance <500 mW/cm^2) was effective at selectively heating blood relative to other tissue types.

The studies presented here demonstrate that enhanced thermal imaging is a promising imaging modality for medical applications that can benefit from imaging blood flow and vascular morphology. Our noncontact method could also be of use for any surgical procedure where avoiding or targeting vascular components is needed. The low cost and reliability of the LEDs make them an attractive alternative to more expensive laser sources. Recent developments in IR detectors have reduced the cost and improved the availability and quality of thermal cameras. Enhanced thermal imaging has the potential to be a low cost, reliable method for medical professionals to provide improved care for their patients.

CHAPTER 3: EX VIVO STUDIES OF SIMULATED BLOOD FLOW

3.1 Introduction

We have demonstrated that an LED source with wavelength near 530 nm can be used to warm blood with respect to water-rich tissue. In this study, we combine the principles of thermal imaging and selective heating to create a method for imaging blood vessels at mid-IR wavelengths. The warmed blood appears brighter in thermal images, providing contrast between the vessels and surrounding tissue.

We have mapped vascular structures in porcine heart tissue samples *ex vivo*. External LED illumination heats blood and the warmed blood flows through the vascular network in the heart tissue. A thermal camera tracks the flow of the warmed blood. We have developed an image processing technique that highlights temporal and spatial variations in temperature and can reveal the location and morphology of subsurface vessels.

3.2 Methods

Two LED sources with peak wavelengths near 530 nm (Thorlabs M530L2) were used to illuminate porcine blood flowing through existing vasculature in a sample of porcine heart tissue (See Figure 3.1).

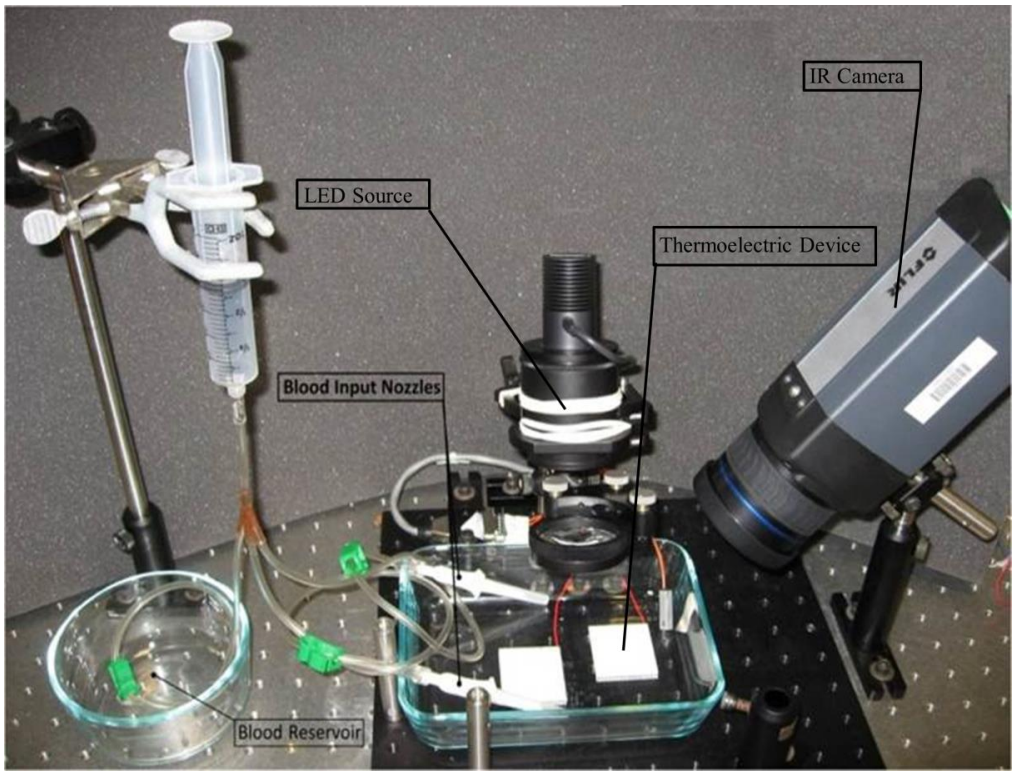

Figure 3.1: Blood flow study equipment.

The LED output was collimated using a 3 lens system producing an approximately 2 mm-diameter spot on the tissue surface. Both 530 nm LED sources operated at maximum power output of 1000 mW for these experiments. The two LED sources simultaneously illuminated the tissue sample. This arrangement yielded an average power density of approximately 680 mW/cm^2 at the tissue surface. The spectral width for each LED was 16 nm. A FLIR SC600 series mid-IR camera (sensitive from 7.5 to 14.0 microns) was used to record the flow of the warmed blood. The camera has an array size of 640 x 480 pixels and a maximum frame rate of 200 fps.

Porcine heart tissue samples and blood were obtained from Animal Technologies, Inc. (Tyler, Texas). The blood was collected from donors sacrificed on the day of shipment and contained EDTA anticoagulant to prevent clotting. The tissue samples were kept hydrated using a saline bath during all experiments. The tissue samples and blood were at room temperature at the start of each experiment.

An IV like setup with a hypodermic needle was used to introduce blood flow into the existing vasculature in a segment of porcine heart tissue. Vessels used for the introduction of blood were chosen by visual inspection. The LED spot was aligned to illuminate the vessel just beyond the point where blood flow was introduced. The blood was heated as it flowed through the LED spot and then continued to flow through the vascular network. The LED continuously illuminated the tissue for as long as the blood flow could be maintained (10-60 seconds). The flow of this warmed blood through the vascular network was monitored with the thermal camera. Five porcine heart tissue samples were studied. Each sample was imaged multiple times (n=3-5 each).

Table 3.1: LED parameters for simulated blood flow

Wavelength (nm):	530
Irradiance (mW/cm^2):	680
Spot Diameter (mm):	2
Mode of LED Illumination	Continuous

3.3 Results

Five heart tissue samples were tested. Here we discuss the results for one sample (Sample 1) in detail as it exhibited the most interesting vessel morphology. Other samples were analyzed in an identical manner and yielded similar results which are summarized in Table 3.1. Figure 3.2A shows a representative mid-IR image of heated blood flowing through existing vasculature in porcine heart tissue. The heated blood and the warm LED spot are clearly visible in this image. The 530 nm LED heated the blood to a temperature of 24.4 °C above a minimum of 23.9 °C. It is important to note that the 530 nm heated the blood to a temperature only slightly higher than the surrounding tissue and was able to reveal vascular detail. The path of the heated blood, and thus the blood vessel, can be seen extending ~ 5 cm from the LED spot. Further than 5 cm from the LED spot, the temperature difference between the blood and surrounding tissue was no longer adequate to visualize the vessel. This vessel could only be followed for 2 cm from the LED spot by visual inspection. After 2 cm, the vessel was below the surface of the muscle tissue. Our enhanced contrast thermal imaging method is capable of tracing vessels 3 cm further than was possible by visible inspection alone.

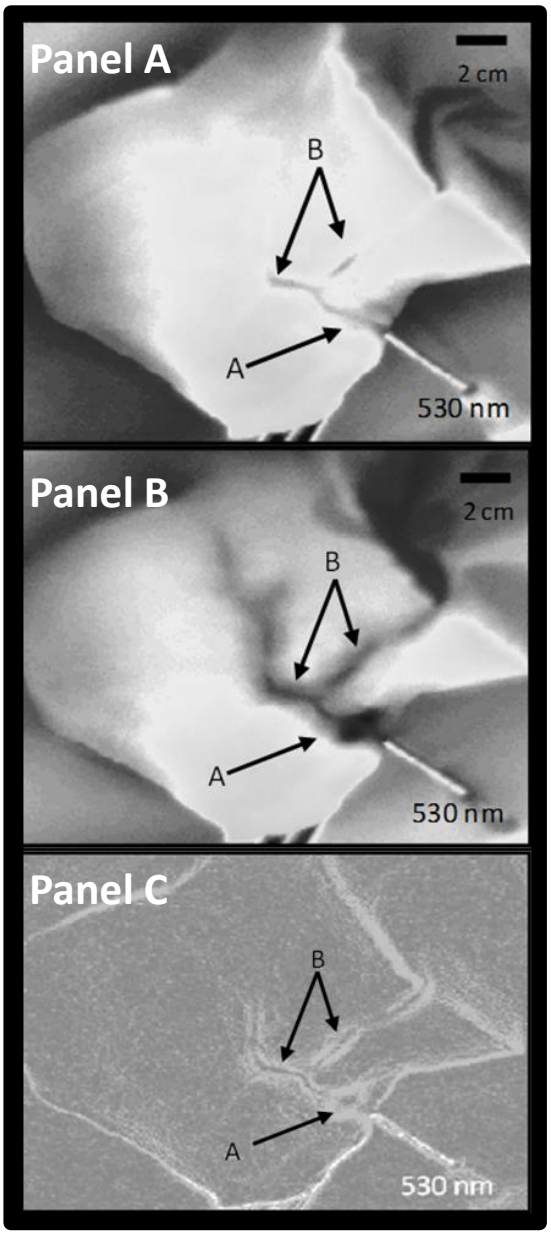

Fig 3.2: *Panel A:* Mid-IR images that show the flow of warm blood through vessels in a section of porcine heart tissue. The arrows highlight the LED spot (A) and warmed blood (B). *Panel B:* By mapping the change of temperature as a function of time, a more detailed image of the vessels is produced allowing the vessels to be seen > 15 cm from the LED spot. These more distant vessels were not seen in the unprocessed thermal images or by visual inspection. *Panel C*: By mapping the change of temperature as a function of position, vessel edges and details were enhanced. The location of these vessels was verified by dissection and found to be at a maximum depth of ~ 0.75 cm.

Warmed blood flowed away from the LED spot into cooler tissue in these experiments. This flow of warm blood into a cooler region results in a rapid change of temperature as a function of time in the region. We applied a time derivative analysis to our images to highlight these rapid changes of temperature. This method emphasized changes in temperature from one frame to the next of the video recorded with the thermal camera. The changes in temperature from frame to frame were summed and then normalized into an image. This analysis highlighted regions where the sample was heated, neglecting regions of small change due to background and noise (See panel B of Figure 3.2). This time derivative map highlights the path of the selectively heated blood through the vascular network during the LED illumination (see Figure 3.2B). Vessels could be followed for 16 cm from the LED spot compared to 5 cm in the unprocessed images.

We also applied a spatial derivative analysis to our images. Using MATLAB the change in temperature was calculated from pixel to pixel. This derivative analysis highlights changes in temperature as a function of position. Figure 3.2C shows the results of the spatial derivative analysis. The spatial derivative reveals the edges of blood vessels and more detailed structures than could be seen in the unprocessed images or time derivative images. We could follow the path of the warmed blood for ~ 10 cm in these images.

After imaging was complete, the tissue was dissected to verify the location of the vessels imaged. The vessel into which blood flow was introduced was at the surface of the tissue near the LED spot and we could see the first 2 cm of the vessel by visual

inspection. Beyond the initial 2 cm the blood vessel was below the tissue surface. Dissection revealed that the vessel was 0.75 cm beneath the surface of the tissue at points 3 and 4 in Figure 3.3. Our thermal imaging method was able to map the vessels for up to 16 cm from the LED spot and at depths up to 0.75 cm below the surface of the heart tissue.

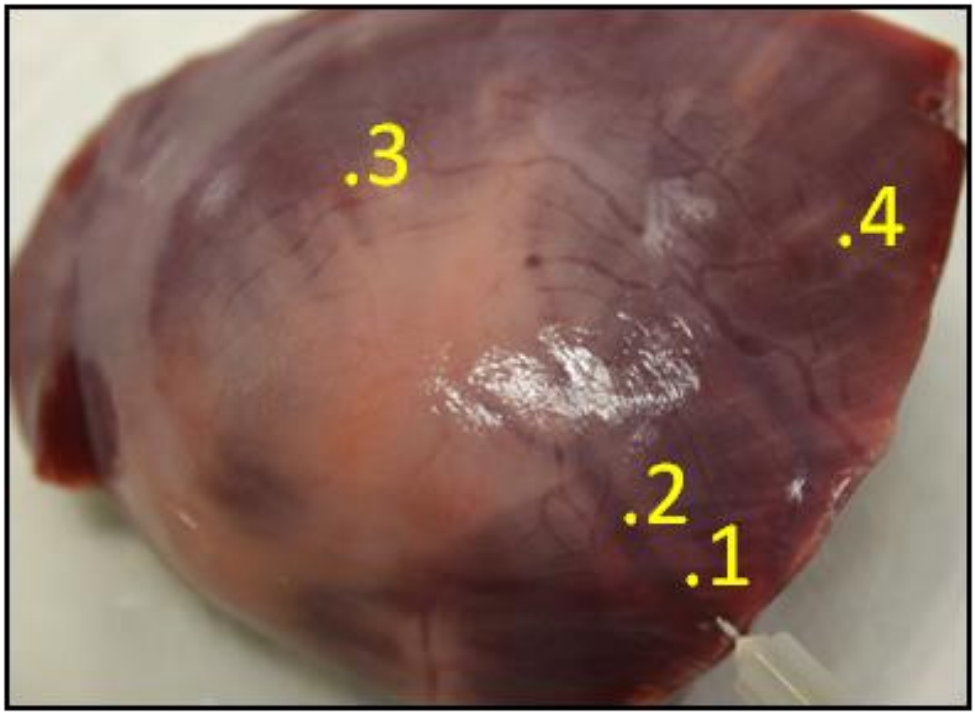

Fig 3.3: Photograph of the heart muscle tested after dissection. In the figure the first part of the vessels is visible. Point 1 marks the entry point of the blood. Point 2 marks the location of the LED spot and points 3 and 4 indicate places at which the vessels were at the maximum imaged depth of 0.75 cm.

Similar measurements were made for all samples tested to determine the capabilities of this imaging method. Table 3.2 lists the depths and distance at which the blood vessels could be imaged using our enhanced mid-IR methodology for each sample. Maximum distances are determined using temporal derivative analysis and maximum depths are determined by dissection. In Table 3.2 values marked with ">" indicates that out imaging method was able to map the vessel until its end.

Table 3.2: Summary of vessel properties reporting the distances our method was able to follow blood flow and the maximum depth reached by the vessels.

Sample #	**Distance [From LED Spot] (cm)**	**Maximum Depth (cm)**
1	16.0	0.75
2	>3.5	0.45
3	>3.8	0.15
4	>2.1	0.13
5	2.3	0.18

3.4 Discussion

Experiments were conducted to simulate blood flow through existing blood vessels in porcine heart tissue. We developed an image processing method that highlights temporal and spatial variations in temperature that allowed the mapping of vessels as deep as 0.75 cm below the tissue surface and up to 16 cm from the location of the LED spot. This study demonstrates that enhanced thermal imaging is a promising imaging modality for medical applications that can benefit from imaging blood flow and vascular morphology.

CHAPTER 4: HEAT TRANSFER MODELS

4.1 Introduction

We have demonstrated that enhanced thermal imaging (selective heating of blood coupled with mid-IR imaging) can map vascular networks in porcine heart tissue. These images provide information about the two dimensional locations of the vessels, but do not provide the depth and size of these structures. In this study, we use heat transfer models developed using COMSOL Multiphysics to create an algorithm that allows 3-D mapping of the vessels seen in the mid-IR images. The study of the biological heat transfer equation is relevant in the field of thermal medicine because experimental temperature data is not widely available.[38] Much of the work to model the transfer of thermal energy in biological tissues focuses on photothermolysis or microwave ablation. For example, COMSOL has been used to model of collateral damage in laser ablation of prostate cancer and also microwave heating of tissue to destroy liver cancer tumors.[39,40] These models do not focus on the time evolution of the thermal surface profile, the main requirement of our algorithm development. For the majority of models developed a finite elements method is used to find solutions[41,42] similar to the methods used by the COMSOL Multiphysics software package.

We determine the depths and sizes of blood vessels based on two quantities: signal arrival time and the surface temperature profile at this arrival time. Ultrasound and

photo-acoustic imaging both use signal arrival time to determine the depths of targets in tissues.[43,44] For example, an ultrasound probe sends a sound wave into tissue and the time it takes for the signal to return to the probe is used to determine the distance to the target. We are using a similar approach to determine depths of blood vessels in enhanced thermal imaging.

In our enhanced thermal imaging technique, an LED heats blood relative to the surrounding tissue and this thermal signal then propagates through the surrounding tissue. It is this thermal signal that we detect at the surface of the tissue in our enhanced thermal images. By determining the time that it takes for this thermal signal to reach the tissue surface from an embedded vessel, we can determine the depth of a blood vessel. In addition, the temperature profile across the surface of the tissue can be used, with the arrival time information, to determine the size of the vessel.

4.2 Methods

4.2.1 Modeling Methods

COMSOL Multiphysics was used to model heat transfer from blood vessels through muscle tissue for comparison with mid-IR images of porcine heart tissue that we obtained in a previous study (see Chapter 3). We also compared them to gelatin based tissue phantoms (See section 4.2.2). A schematic of the geometry used in the model is shown in Figure 4.1.

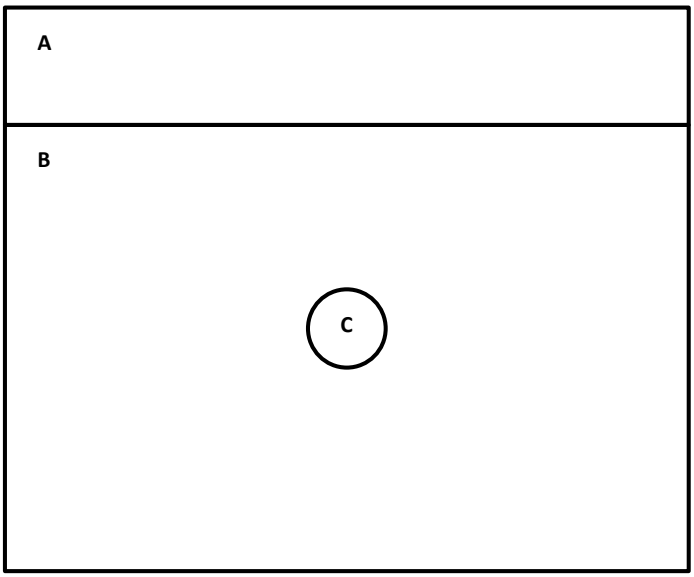

Figure 4.1: COMSOL Model Geometry. Region A is a 10 by 50 mm area of still air. Region B is muscle tissue with a width of 50 mm and height of 40 mm. Region C is modeled as whole blood with radii that were varied from 0.25 to 2.0 mm. Heat is allowed to flow across all outer boundaries.

We modeled the muscle tissue as a slab and then embedded a circular vessel. The thickness of the slab was 10 mm and the width was 50 mm. Heat was allowed to flow across the boundaries along the top, bottom and sides of the muscle tissue to approximate an infinite slab. A thin (10 mm) region of static air held at a constant temperature of 37 °C was placed at the top of the muscle tissue to more closely replicate an open surgery where the muscle surface would be exposed to air. Fluid movement of the air region was not considered in this set of models and will be included in more realistic models in future work. Also the muscle and air were set in initial thermal equilibrium to eliminate any changes convective cooling may have of the thermal profiles. The goal of these models was to understand how the thermal signatures behaved as a result of vessel

heating only. At t=0 in the model, the muscle tissue was set to an initial temperature of 37 °C and the vessel temperature was set to be 1-2 degrees above the muscle temperature. These initial studies did not include the LED illumination as the source of heating. We simply set the temperature of the vessel to a constant temperature above the surrounding tissue to mimic the heating caused by LED illumination. The model then followed the heat transfer for 60 seconds. We varied the depth and size of the vessel by changing the radius and position of the blood in the muscle. Table 4.1 lists the thermal properties of materials used in these models which were obtained from COMSOL's database of known materials.

Table 4.2 shows a complete list of the sizes/depths of vessels that were modeled. We modeled vessel radii ranging from 0.25 mm to 2.0 mm embedded at depths ranging from 1 mm to 10 mm (at 1 mm increments) in muscle tissue. We also modeled each of these vessel/depth combinations at three different temperatures relative to the surrounding tissue: 1 °C, 1.5 °C and 2 °C warmer than the surrounding muscle tissue. MATLAB was used to determine the time at which the thermal signal arrived at the surface by detecting the moment at which the surface temperature increased by 0.01 °C above the initial temperature. This arrival time was noted and the surface temperature profile at this time was saved for further analysis.

Table 4.1: Thermal Properties of Modeled Materials.

Material	Heat Capacity (J/Kg•K)	Density (Kg/m^3)	Thermal Conductivity (W/m•K)
Muscle	3421	1090	0.49
Blood	3617	105	0.52
Air (@40 °C)	1005	1.127	0.027

Table 4.2: Vessel Depths and Sizes Modeled.

Vessel Radius, R [mm]	Vessel Depth, D [mm] (ΔR=1)	Temperature Difference, T [°C] between vessel and muscle, (ΔT=0.5)
0.25	1:10	1:2
0.5	1:10	1:2
0.75	1:10	1:2
1.0	1:10	1:2
1.5	1:10	1:2
2.0	1:10	1:2

4.2.2 Tissue Phantoms

A series of tissue phantoms (n=18) were developed to test high-intensity focused ultrasounds. Gellan gum (CG-LA, CP Kelco, Atlanta, GA) was used to as the base for these phantoms because of its high temperature resistance (melting point > 100 °C), mechanical strength and better clarity than other available gelatin types. After mixing the

phantoms according to the recipe, shown in appendix A, resistive wires of various diameter were placed at various depth within the fluid mixture. After the phantom was allowed to cure electrical current was applied to each wire individually and the resulting heating was recorded at the surface with the FLIR mid-IR camera.

4.3 Analysis and Results

Arrival times were determined for each model. Figure 4.2 shows a representative plot of signal arrival time (an output of the model) versus vessel depth (this was a parameter set in the model) for a vessel with a radius of 1.0 mm. As expected, it took longer for the thermal signal to arrive at the tissue surface when the vessel was more deeply embedded. Figure 4.3 shows arrival time versus depth for a range of vessel sizes. Notice that signal arrival time is not completely independent of vessel size. Larger vessels produce a stronger thermal signal and we detect the arrival for this signal more quickly than for smaller vessels at the same depth. Recall that we are defining the arrival time as the moment at which the surface temperature increases by 0.01 °C from the initial temperature. The stronger thermal signal from a larger vessel more quickly causes this temperature increase than the signal from a small vessel. This effect is especially noticeable for deeply embedded vessels.

In the models we set the initial temperature difference between the vessel and muscle to three different values: 1 °C, 1.5 °C and 2 °C. Figure 4.4 shows signal arrival time versus vessel depth for a vessel with a radius of 1.0 mm at these three different temperatures. As the temperature of the vessel increases the arrival time decreases. The warmer vessels produce a stronger thermal signal that can cause the 0.01 °C surface

temperature increase more quickly. This is a similar effect as was seen for a larger vessel having a faster arrival time. Signal arrival time depends primarily on vessel depth, but does have a dependence on vessel size and the temperature difference between the vessel and surrounding tissue, especially for deeply embedded vessels.

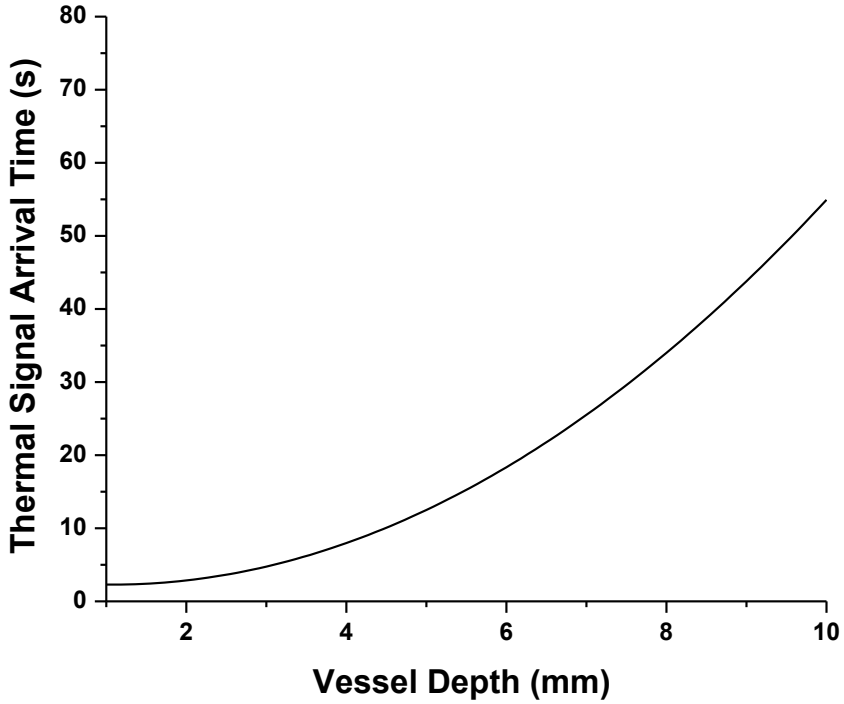

Figure 4.2: Arrival time versus depth for a 2 mm vessel embedded in muscle tissue. As depth increases, the time for the thermal signal to arrive at the surface increases. Signal arrival time can be used to determine vessel depth.

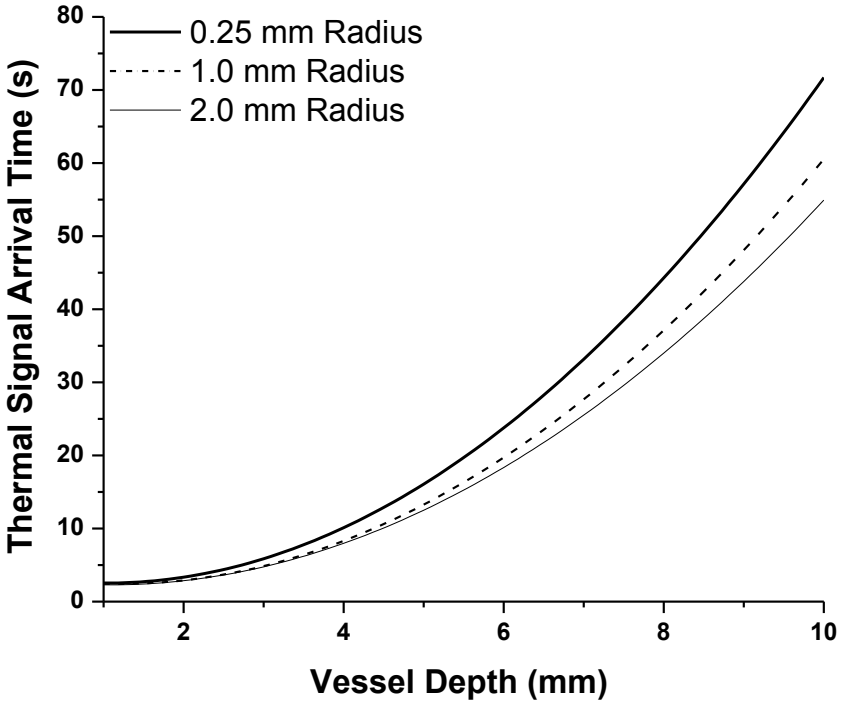

Figure 4.3: Arrival time versus depth for vessels with different radii. Arrival time does depend on vessel size for deeply embedded vessels.

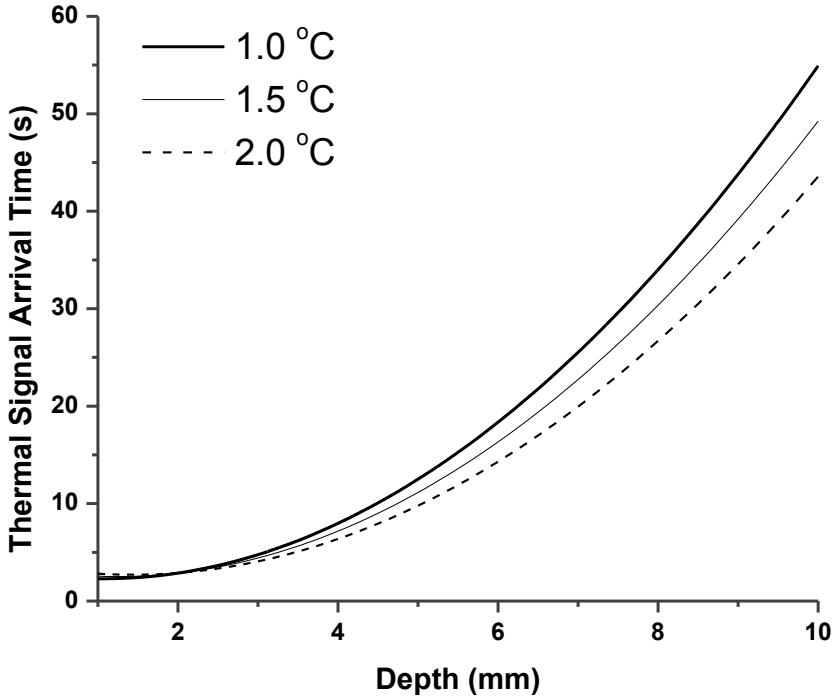

Figure 4.4: Arrival time versus depth for a 2 mm vessel at different initial temperatures with respect to surrounding muscle tissue. Arrival time depends on this temperature difference, especially for deeply embedded vessels

Figure 4.5 shows a representative thermal profile of the tissue surface at the signal arrival time (vessel depth = 3 mm and vessel size = 1 mm). The profile is approximately Gaussian in shape for all models. The spatial derivative of the profile was used to determine the width of the profile. This method was much faster than fitting a Gaussian profile and accomplished the same task. The distance between the maximum and minimum of the derivative of the profile was measured and recorded as the peak width (see Figure 4.6).

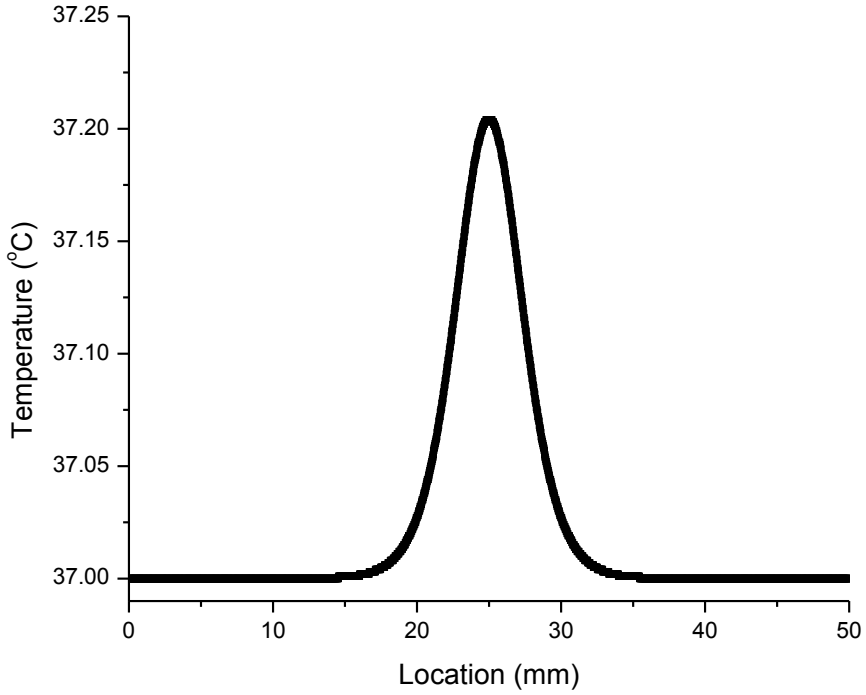

Figure 4.5: Representative thermal surface profile for a 1 mm vessel at a depth of 3mm. This plot shows the thermal profile just after the signal arrival.

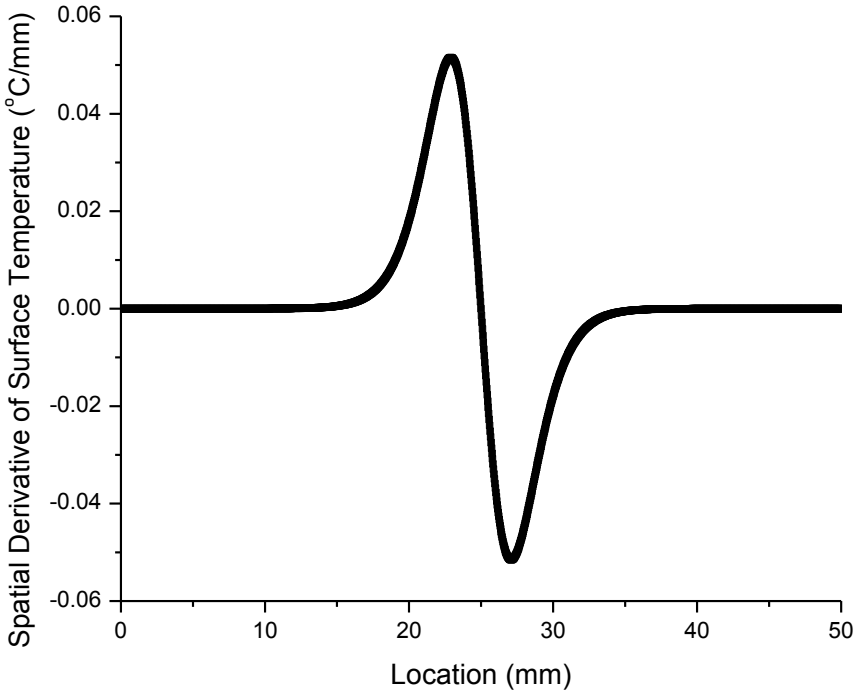

Figure 4.6: Representative plot of the derivative of the thermal surface profile for a 1mm vessel at a depth of 3 mm. The separation of the two peaks was used to estimate the width of the thermal profile.

The width of Gaussian profile is related to the size and depth of the vessel. Figure 4.7 shows the relationship between the peak width and vessel size at a fixed depth (depth = 2.0 mm). All vessel radii showed similar trends. The peak width increases approximately linearly with increasing vessel radius. Figure 4.8 shows the relationship between the peak width and vessel depth at a fixed size (radius = 1.0 mm). All vessel radii showed similar trends. The peak width increases approximately linearly with increasing depth.

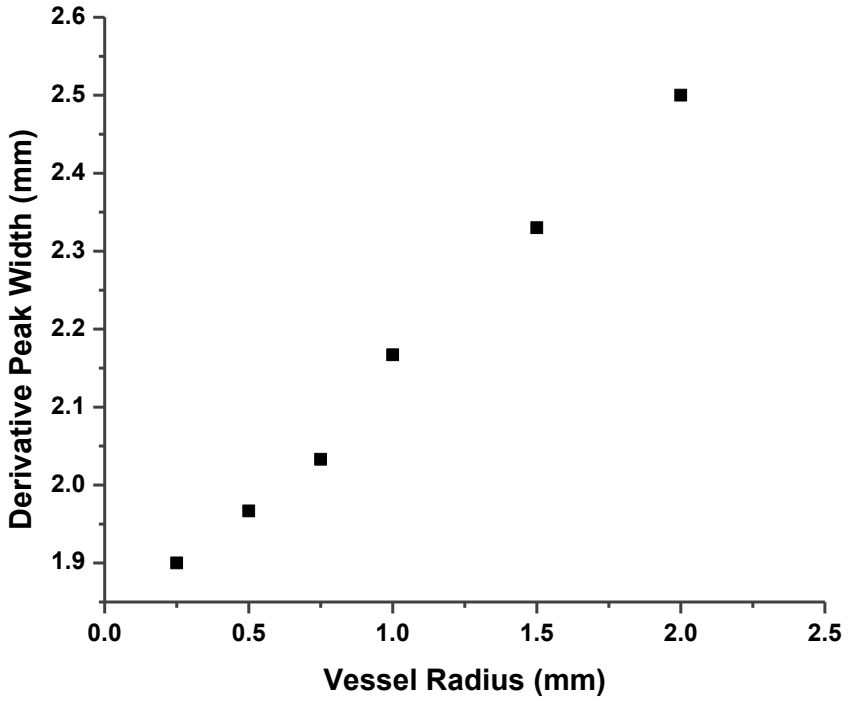

Figure 4.7: A representative example of peak width versus vessel radius at a fixed depth (depth = 2.0 mm). As the vessel size increases the peak width increases approximately linearly.

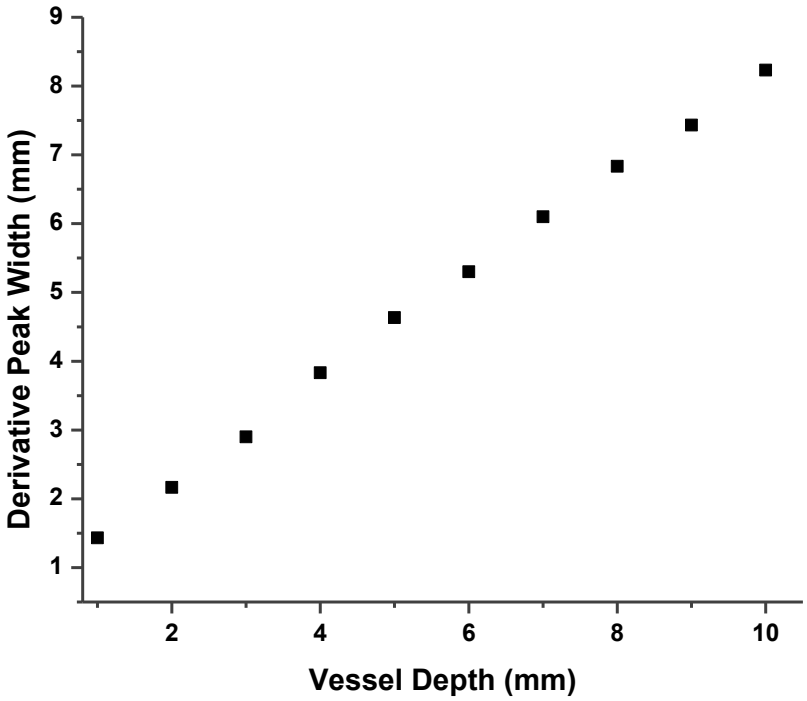

Figure 4.8: A representative example of peak width versus vessel depth for a fixed vessel radius (radius = 1.0 mm). As the depth increases the peak width increases approximately linearly.

4.4 Algorithm for Determining the Size and Depth of Vessels Embedded in Muscle Tissue and Comparison to Experimental Thermal Imaging Results

The signal arrival time and the surface profile can be used to estimate the size and depth of a blood vessel. We first determine the approximate depth of the vessel based on the signal arrival time. Next, we use the depth coupled with the peak width of the thermal surface profile to determine the vessel size. Figure 4.9 outlines the basic steps of this algorithm.

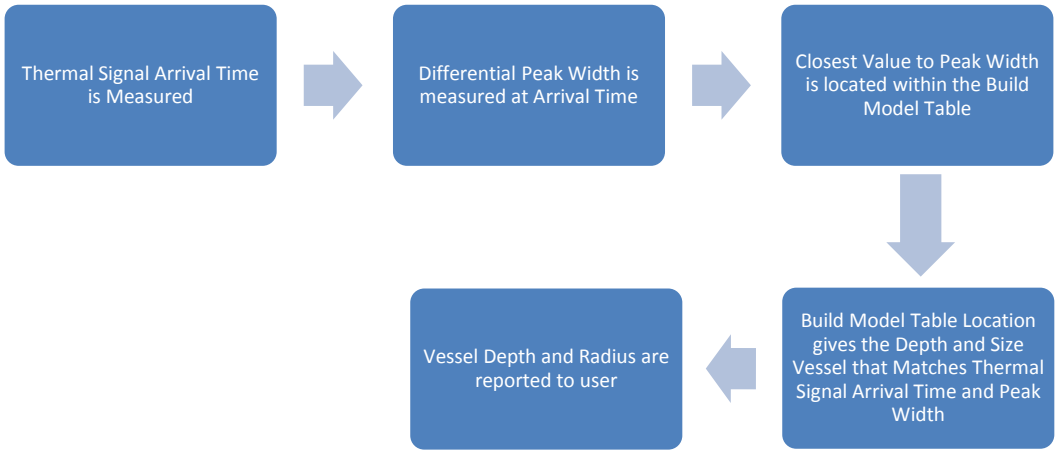

Figure 4.9: This flow chart shows the basic steps of the algorithm to determine depth and size of an imaged vessel.

We compiled a look-up table based on model results in order to test this algorithm against thermal images of porcine heart tissue. Signal arrival times and derivative peak widths were determined for all models, covering a range of vessels\ depths and sizes (see Table 4.2). A linear interpolation was used to fill in values between the modeled results in the look up table. Figure 4.10 shows a small excerpt from the lookup table and demonstrates the basic concept behind the depth/size determination. Once arrival time is determined, a range of allowed depths (shown in blue in Figure 4.10) is found using the lookup table. Signal arrival time is a function of vessel size and the temperature difference between the vessel and surrounding muscle tissue (as seen in Figures 4.2-4.4). This results in a range of possible depths for a given arrival time, rather than a single

depth value. The closest value in the table to the measured peak width within the allowed depth range is then determined.

		Vessel Radius (mm)								
		0.25	0.25117	0.25233	0.2535	0.25467	0.25584	0.26051	0.26167	0.26284
Vessel Depth (mm)	1	1.16661	1.16707	1.16753	1.16799	1.16845	1.16891	1.17075	1.17121	1.17166
	1.09091	1.23766	1.23811	1.23857	1.23903	1.23948	1.23994	1.24177	1.24222	1.24268
	1.18182	1.3087	1.30915	1.30961	1.31006	1.31052	1.31097	1.31279	1.31324	1.3137
	1.27273	1.37974	1.3802	1.38065	1.3811	1.38155	1.382	1.38381	1.38426	1.38472
	1.36364	1.45079	1.45124	1.45169	1.45214	1.45259	1.45304	1.45483	1.45528	1.45573
	1.45455	1.52183	1.52228	1.52273	1.52317	1.52362	1.52407	1.52586	1.5263	1.52675
	1.54545	1.59288	1.59332	1.59376	1.59421	1.59465	**1.5951**	1.59688	1.59732	1.59777
	1.63636	1.66392	1.66436	1.6648	1.66525	1.66569	1.66613	1.6679	1.66834	1.66878
	1.72727	1.73496	1.7354	1.73584	1.73628	1.73672	1.73716	1.73892	1.73936	1.7398
	1.81818	1.80601	1.80644	1.80688	1.80732	1.80776	1.80819	1.80994	1.81038	1.81082
	1.90909	1.87705	1.87749	1.87792	1.87836	1.87879	1.87923	1.88097	1.8814	1.88184
	2	1.9481	1.94853	1.94896	1.94939	1.94983	1.95026	1.95199	1.95242	1.95285

Figure 4.10: Part of the look up table used to determine vessel depths and sizes. A range of possible depths is determined based on signal arrival time (shown in blue). Peak width at this depth is then used to determine vessel size.

The algorithm developed using this model was applied to profiles obtained from other depth and size COMSOL models and the algorithm's predictions yielded a zero percent error as expected. Next the method was applied to a study gelatin based tissue phantoms that have been shown to have similar thermal properties to soft tissue (See Appendix A).[45] The thermal signal arrival time and derivative peak width was determined for each vessel phantom. This information was then used to determine the depth and radius as predicted by algorithm. Table 4.3 list the measured and predicted values for all phantoms tested with their associated percent error.

Table 4.3: Phantom Results. This table lists the measured and values predicted by our algorithm and any associated percent errors.

Actual		***Predicted***		***% Error***	
Depth	**Radius**	**Depth**	**Radius**	**Depth**	**Radius**
0.65	0.35	0.81	0.52	24.62	48.57
0.7	0.6	1.46	0.48	108.57	20
1	0.6	2.15	0.63	115	5
1.2	0.75	2.38	0.85	98.33	13.33
1.3	0.75	1.92	0.788	47.69	5.07
1.4	0.75	2.15	0.8	53.57	6.67
1.55	0.35	2.62	0.25	69.03	28.57
1.6	0.35	1.46	0.46	8.75	31.43
1.9	0.6	1.46	0.71	23.16	18.33
5.3	0.35	8.15	0.67	53.77	91.43
6.35	0.35	8.38	0.81	31.97	131.43
7.2	0.6	8.15	0.67	13.19	11.67
7.25	0.75	7.46	0.77	2.9	2.67
7.35	0.75	9.3	0.73	26.53	2.67
7.5	0.6	7.69	0.46	2.53	23.33
7.7	0.6	7.92	0.56	2.86	6.67
8.2	0.75	8.39	0.81	2.32	8
8.3	0.35	8.62	0.44	3.86	25.71

Our algorithm is capable of predicted the size and depth of the embedded heated wires. The errors are a result of experimental thermal signal arrival time measurements. Measuring the arrival time for shallower wires proved to be challenging and the wires did not heat instantaneously, delaying the arrival time.

The algorithm was finally applied to *ex vivo* blood flow studies (see Chapter 3 for a description of data acquisition). For the *ex vivo* studies signal arrival time was estimated by measuring the temperature in the mid-IR images from the flow studies. Once the surface temperature change was equal to approximately 0.01 °C, the time elapsed between the start of LED illumination and this temperature change time was recorded as "arrival time". This was done for multiple cross-sections of each tissue sample to estimate the vessel size and depth at multiple locations. Once these measurements were completed all tissue samples were dissected into cross-sections corresponding to the locations at which arrival time was determined. Vessel depths and radii were measured with vernier calipers.

Table 4.4 lists the measured and predicted values, with percent error, for ten different vessel locations from the *ex vivo* flow studies. Errors were largest for shallow vessels (depth < 2 mm), while depth determinations for deeper vessels were more accurate.

In the *ex vivo* flow studies, blood was heated by the LED and then flowed into the vascular network. This experimental setup introduced error into our determination of signal arrival time, and thus vessel depth. This error affected shallow vessels more

because the short arrival times were more difficult to measure. Errors in estimated radii of vessels were smaller as peak width was not as sensitive to the experimental error.

Table 4.4: Measured and predicted vessel depths and sizes for ex vivo studies.

	Actual		**Predicted**		**% Error**	
Sample	Depth	Radius	Depth	Radius	Depth	Radius
8	0.85	0.575	2	1.18	135.3	105.2
6	1	1.15	4	1.28	300	13
7	1.25	0.775	5	0.59	300	23.8
9	1.25	0.7	2	1.18	60	68.5
2	1.45	0.375	2	.348	37.9	7.2
5	1.5	0.55	4	0.86	173.4	56.3
1	2.15	1.15	2	1.242	6.9	8
10	2.35	1.15	4	1.93	70.2	67.8
3	3.55	1.5	3	1.164	15.5	22.4
4	4.45	0.6	5	0.599	12.4	0.1

4.5 Conclusions

We used COMSOL Multiphysics to model heat transfer from heated blood vessels through muscle tissue. These models were used to determine the relationship between vessel size and depth with thermal signal arrival time and thermal surface profiles. Signal arrival time is dependent primarily upon the depth of a vessel. The thermal profile

depends on both the depth and size of the vessel. Based on the model results, we developed an algorithm to determine vessel size and depth.

The algorithm developed using these models was applied to gelatin tissue phantoms and the *ex vivo* flow studies presented previously in Chapter 3. The phantom results were favorable displaying errors that were expected due to the idealized nature of the models used to build the look up table. From the *ex vivo* test we were successful at predicting depths and sizes for vessels embedded deeper than 2 mm in muscle tissue. More extensive modeling with more realistic tissue properties (e.g. layered structures, inhomogeneities, etc.), and the application of an iterative process, will improve the accuracy of our algorithm.

CHAPTER 5: NON-INVASIVE MID-IR DETECTION OF BREAST TUMOR DEVOLOPMENT *IN VIVO*

5.1 Introduction

The American Cancer Society estimates that 231,840 women and 2,350 men will be diagnosed with breast cancer and that 40,730 will die from the disease in 2015.[46] Lumpectomy coupled with radiation therapy and/or chemotherapy is the treatment undergone by many breast cancer patients.[47] While mammography is a reliable imaging method for the detection of breast cancer, it cannot be used in real-time during surgical procedures to guide tissue excision. Currently X-ray, MRI and/or ultrasound images of the breast are taken prior to surgery and used as a reference during the procedure. During a lumpectomy, the tumor is removed and the tumor margins are immediately tested for the presence of cancer cells via frozen section histology. If cancer cells are found in the margins, additional tissue may be removed. This process can lead to a prolonged or multiple procedures which increases the risk of surgical complications.[48] New methods such as photoacoustic (or optoacoustic) imaging and fluorescent imaging are being investigated to allow real time optical biopsies. However, these methods often have a limited field of view and/or are time consuming.[49] We are developing an imaging method capable of imaging a large area of tissue in one acquisition to define excision margins in real-time during lumpectomy.

The development of new vascular structures, or angiogenesis, provides the nutrients and oxygen needed to support tumor growth and plays a key role in the generation of metastasis.[50] The location of vascular structures associated with breast cancer tumors is one of the criteria that help define tumor margins. Enhanced thermal imaging is designed to detect these vascular networks associated with tumor growth. Our technique is a combination of thermal IR imaging (8-10 μm) and selective heating of blood (~0.5 °C) relative to surrounding water-rich tissue using LED sources at low powers. Generating enhanced contrast in thermal images is essential for the success of the technique. Blood absorbs light strongly at 530 nm, while absorption by soft tissues is lower at this wavelength.[51] Illumination of tissue containing vessels with a 530 nm light source heats the blood (by < 1 °C) compared to surrounding tissues. The warmer blood appears brighter in thermal images, providing contrast between the vessels and surrounding tissue. We have already successfully mapped vessels 1-2 cm below the surface of porcine muscle tissue.[52] This method does not require injection of contrast agents or direct contact with the tissue.

In the present study, the growth of breast cancer tumors in the 4T1 murine orthotopic model was monitored in vivo using enhanced thermal imaging. The results of the enhanced thermal imaging are compared to fluorescent and standard thermal imaging of the same subjects as well as physical caliper measurements of tumor sizes to test the validity of using enhanced thermal imaging to monitor tumor growth. We also investigate the feasibility of using enhanced thermal imaging to estimate tumor margins.

5.2 Methods

5.2.1 Murine Tumor Model

Nineteen Balb/c female mice 5-6 weeks old (20-23 grams) were purchased from Jackson laboratories and acclimatized to the Vivarium at UNC Charlotte prior to use. All experiments were approved by the Institutional Animal Care and Use Committee at UNC Charlotte and supervised by the staff veterinarian. On Day 1 of the study, animals were implanted with 5 x 104 4T1-RFP (Excitation 558 nm – Emission 583 nm) breast cancer cells (AntiCancer, Inc.; San Diego, CA) within the mammary fat pad. The injected cells used are aggressive murine mammary cancer cells syngeneic of Balb/c that mimic the later stages of breast cancer in humans. Subjects were fed per oral either saline or the angiotensin receptor antagonist Loasartan (10-15 mg/kg/day; Sigma Aldrich, St Louis MO). Animals were weighed and tumor growth was monitored using calipers every 3-4 days. At Day 30 post tumor implantation, animals were euthanized and the organs and tumors were collected.

Table 5.1: Measurement Frequency. Days on which each type of measurement were conducted.

	Study Day												
Method	1	7	8	11	13	14	17	20	21	23	24	28	30
Caliper			•	•		•	•		•		•		•
IVIS	•		•			•	•		•		•		•
Standard Thermal Imaging	•	•			•		•	•		•		•	
Enhanced Thermal Imaging	•	•			•		•	•		•		•	

5.2.2 Physical Caliper Measurement

The physical sizes of tumors for all mice were measured with calipers throughout the study. Every 3-4 days the length and width of the tumors was measured and recorded. This method could only be used to monitor tumor growth after the tumor was large enough to be palpable (Day 8). Table 5.1 lists the study days on which caliper measurements were collected.

5.2.3 Fluorescent Imaging

All studies were performed using an IVIS Spectrum in vivo imaging system (Perkin Elmer; Waltham, MA). Sedated mice were illuminated and imaged from above (epi-illumination). Four subjects were imaged simultaneously. The fluorescent response was recorded using a 2048 x 2048 cooled (-90 °C) CCD detector (dark current < 100 electron/s/cm2 and RN < 5 electrons for 8 pixel binning). A 25 cm by 25 cm field of view (FOV) was used for all imaging sessions, resulting in a spatial resolution of 0.4 mm in all images. The 4T1-RFP tumor cells used in this study expressed the dsRed2 fluorescent protein with excitation and emission wavelengths of 558 nm and 583 nm, respectively. IVIS imaging was performed using a series of narrow-band filters to isolate the fluorescent signal from the cells while allowing removal of the fluorescence background. This spectral fluorescence background removal was performed using Living Image software.[53] In addition to the fluorescent emission images, low light level white light images of the mice were obtained. The fluorescent images were overlaid with the white light images to correlate the position of the tumor (seen by visual inspection late in the

study) and the fluorescent emission. Table 5.1 lists the study days on which IVIS images were collected.

5.2.4 Enhanced Thermal Imaging

Enhanced thermal imaging is a combination of IR imaging (8-10 microns) and LED illumination to induce a thermal contrast in the samples.[52] Figure 5.1 shows a schematic of the experimental setup. A FLIR SC600 series mid-IR camera (sensitive from 7.5 to 14.0 microns) with an array size of 640 x 480 pixels and maximum frame rate of 200 fps was used to image all mice. A compound germanium lens system with an effective focal length of 100 mm was used with the camera, yielding a spatial resolution of 0.26 mm. Two LED sources with a peak wavelength of 530 nm (Thorlabs M530L2) were used to illuminate the subjects during imaging. The LED sources have a maximum power output of 1000 mW and spectral width of 16 nm. The output from each LED was collimated using an aspheric optic and the LED sources were controlled using a high power LED driver (Thorlabs DC2100). The illumination area had a 4 cm diameter yielding an average power density of 283 mW/cm2.

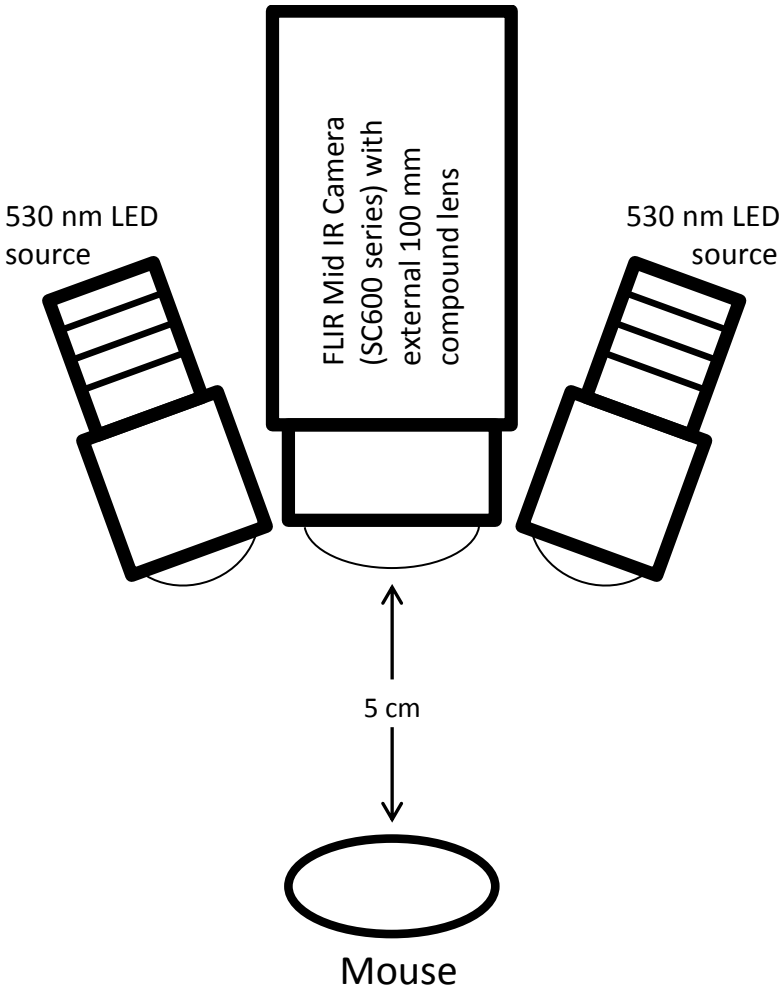

Figure 5.1: The enhanced IR imaging technique uses a FLIR SC600 series camera and two 530 nm Thorlabs LED sources. This configuration yielded a working distance of approximately 5 cm and a spatial resolution of 0.26 mm. The LED sources are used to create a temperature contrast in thermal images by selectively heating blood while the mid-IR camera captures these changes for analysis.

Images were taken on Day 1 both before and immediately after the injection of breast cancer cells and then periodically throughout the study (see Table 5.1). The mice were placed under anesthesia so that they remained stationary during all imaging

sessions. During each imaging session, 4 sets of enhanced thermal images were acquired for each subject. For each image set, the tumor and surrounding tissue were illuminated with the LED sources for 10 seconds. The thermal camera recorded the temperature of the tumor and surrounding area before, during and after LED illumination. The imaging sets were separated by 15 seconds to insure cooling of the tissue. LED illumination heated the blood/vascular networks around the tumor regions by approximately 0.5 °C. This selective heating provided contrast in the thermal images but was well below the tissue damage threshold.[25] During imaging a stainless steel washer was placed on the subject's abdomen just forward of the urethra to aid with image alignment in post-acquisition processing.

5.2.5 Standard Thermal Imaging

In addition to enhanced thermal images, standard thermal images were also obtained to monitor tumor development. No LED illumination was used when these images were taken (i.e., there was no selective heating of blood or blood vessels). The thermal camera recorded the natural temperature gradients across the tumor and surrounding tissue. These thermal images were obtained using the same camera (FLIR SC600) and experimental setup as was used for enhanced thermal imaging. All images used for the purpose of standard thermographic analysis were captured in the first 5 seconds of each imaging session. The first 5 frames from this period were averaged into a single image and a noise reduction was applied using MATLAB. Table 5.1 lists the study days for which standard thermal images were obtained.

5.2.6 Histology

The tumors generated by 4T1-RFP tumor cells were excised 30-days post-implantation. Prior to euthanasia and tumor collection, animals were injected with FITC-dextran to evaluate the blood distribution in and around the tumor. Following collection, tumor masses were fixed in formalin (Sigma-Aldrich, St Louis, MO), embedded in paraffin and serial sections (5-8 μm) were obtained.[54] Tumor slides were stained with Hematoxylin and Eosin to delineate the edge of the tumor mass. Both the tumor mass and its edges and the presence of FITC dextran fluorescence within the tumor mass and the surrounding tissues were assessed based on multiple microphotographs obtained for each tumor mass using a (fluorescent for FITC) microscope and a DP70 camera.

5.3 Results

5.3.1 Estimates of Tumor Volumes

To monitor tumor growth, the volume of the tumor was calculated following the method described by Feldman et al. (see Equation 5.1).[55] The tumor volume was estimated from the area and/or the two-dimensional major and minor axes of the tumor as measured in the IVIS, enhanced thermal and standard thermal images.

Equation 5.1: Feldman Volume

$$V = \frac{\pi}{6} f(Length * Width)^{\frac{3}{2}}$$
$$f = 1.58 \pm 0.01 \ \ (Female\ Mice)$$

An average tumor volume of all subjects (n=19) was calculated on each day that imaging was performed. Errors were estimated based on the standard deviation of the mean.

5.3.2 Physical Caliper Volumes

Calipers were used to physically measure the length and width of tumors from day 8 (i.e. once the tumor mass was identifiable) forward until the end of the study. Tumor volumes, based on the measured lengths and widths, were calculated using the Feldman equation (see Equation 1). As expected, the average tumor volume derived from caliper measurements exponentially increased as a function of time (Figure 5.2).[56]

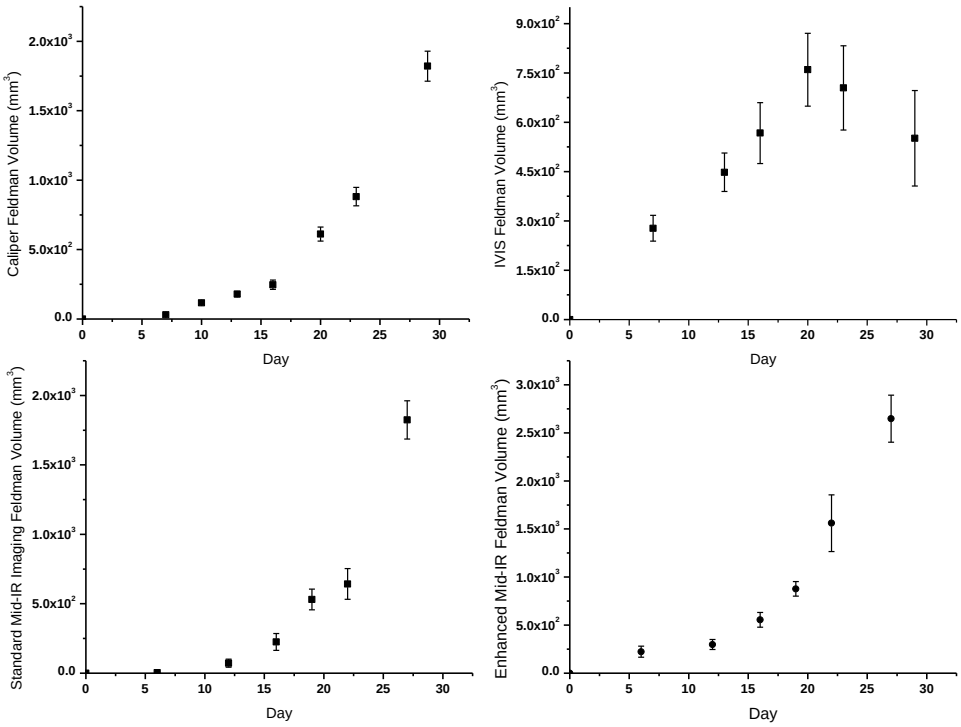

Figure 5.2: Average tumor volume (n = 19) as a function of time for all measurement techniques. Errors are standard deviation of the mean. a) Volumes based on caliper measurements. Approximately exponential tumor growth is evident throughout the study. Measurement before Day 8 was not possible because the tumors were not palpable. b) Tumor volumes derived from IVIS imaging. Exponential growth is observed during the first 22 days of the study. However, after day 22, volumes decrease due to tumor cell necrosis and fluorescent signal loss. c) Average tumor volume based on the standard thermal images. Approximately exponential tumor growth is evident during all days of the study. Images were not taken before day 7. d) Tumor growth as measured by enhanced thermal imaging showing exponential tumor growth from day 7 forward.

5.3.3 IVIS Fluorescent Imaging

Figure 5.3 shows a representative IVIS image (taken on day 14) in which fluorescent emission from the tumor mass is clearly visible. The number of pixels exhibiting fluorescent emission was determined using MATLAB for each mouse. This

pixel area was then used as the elliptical area (length x width term) in the Feldman formula for tumor volume (see Equation 1).

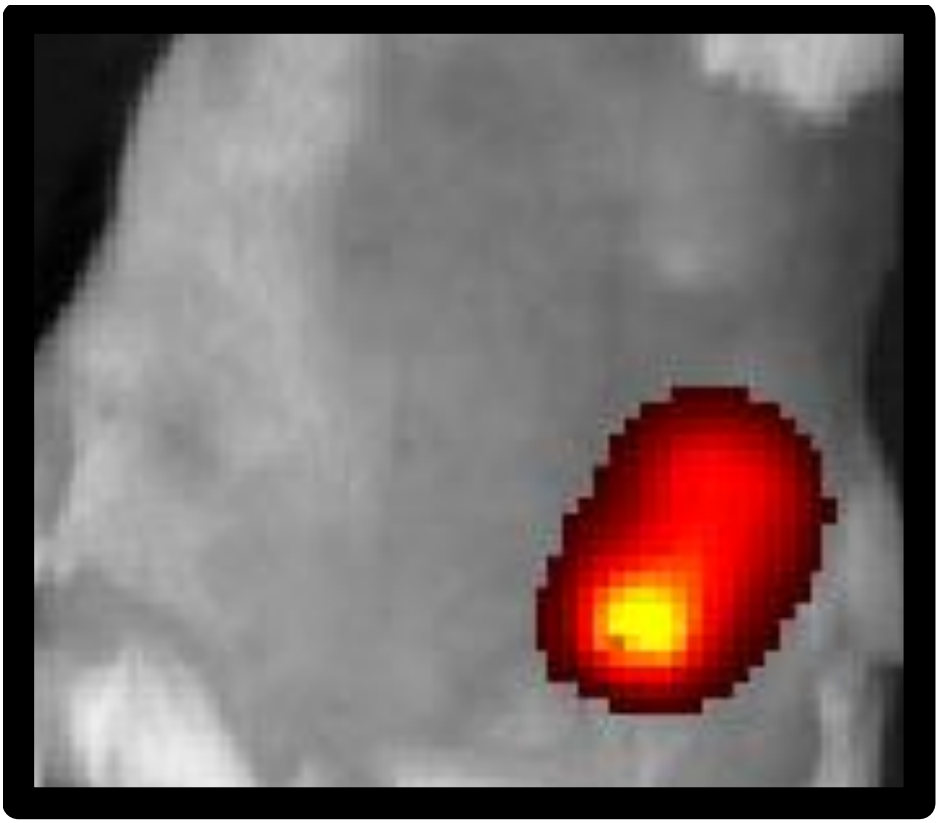

Figure 5.3: Representative example of IVIS images showing fluorescent emission from tumor cells. Regions exhibiting fluorescent emission are shown in false color. The strongest signal (yellow) is associated with the location of the most RFP proteins. IVIS images collected for each mouse on multiple days were used to evaluate tumor area (fluorescently emitting region) and derive tumor volumes.

Average tumor volume as a function of time is shown in Figure 5.2. As expected, IVIS imaging detected the presence of 4T1-RFP expressing cancer cells on the day that the cells were implanted. The tumor volume determined from the 4T1 cell fluorescence was approximately exponential from day 1 to day 22. After day 22 the tumor volume, as

calculated from the IVIS images, begins to decline. Necrosis was observed in all tumor masses from day 22 forward (see Figure 5.4). The fluorescent signal detected by the IVIS imaging system is proportional to the overall number of cancer cells expressing the fluorescent protein. After the tumor masses began to exhibit necrosis, IVIS imaging recorded a smaller fluorescent emission signal due to a decrease in the number of tumor cells expressing the fluorescent protein. In addition, as the tumor mass increases in size, fluorescent excitation of the cells deep in the tumor mass becomes difficult and this may also contribute to the lower emission levels late in the study.

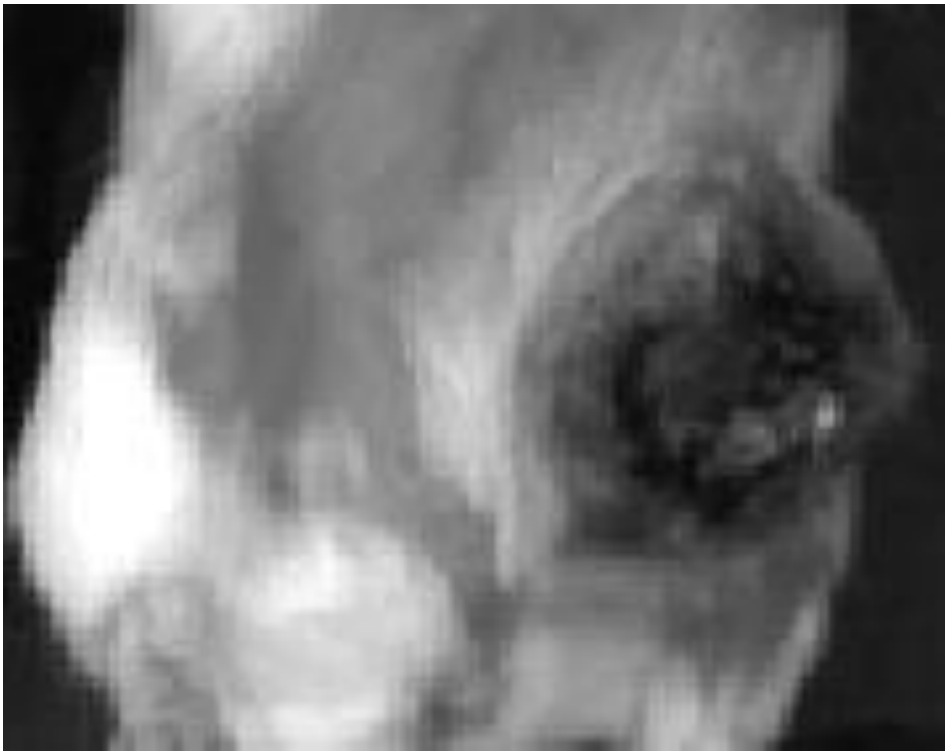

Figure 5.4: A representative white light image taken with the IVIS system showing a necrotic area within the tumor mass (image is from day 25).

5.3.4 Standard Thermal Imaging

Standard thermal imaging was used to monitor tumor growth after day 7 post-tumor implantation. No LED illumination was used when these images were taken (i.e. there was no selective heating of blood or blood vessels). Standard thermal imaging is sensitive to natural temperature differences between the tumor mass and the surrounding tissue. A representative thermal image obtained on day 28 of the study is shown in Figure 5.5. The tumor is clearly visible (the light blue region) but the tumor edges are poorly defined. The tumor mass is about 1 °C cooler than the surrounding healthy tissue, likely due to necrosis and poor perfusion of the tumor at this late stage of the study. The x and y axes of the tumor were estimated using MATLAB and an average tumor volume (n=19) was calculated. The tumor volume increases exponentially with time (see Figure 5.2), consistent with the caliper measurements.

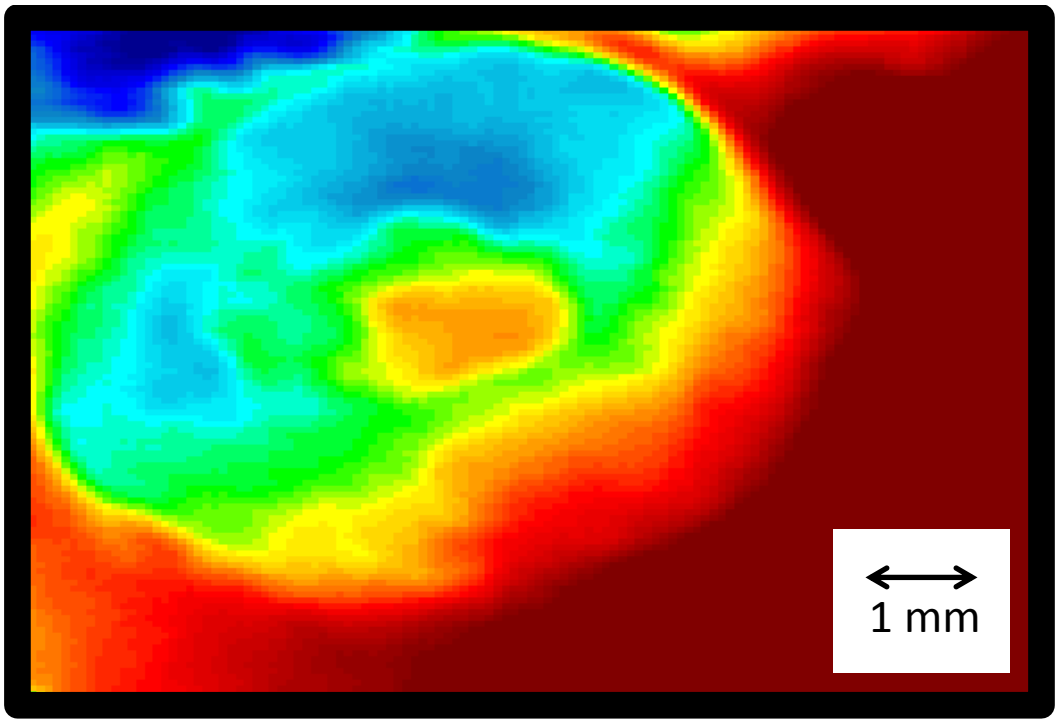

Figure 5.5: Representative standard thermal image of a tumor on day 28 post-tumor implantation. The temperature of the tumor mass (blue/green) is approximately 1 °C cooler than that of the surrounding healthy tissue (red). Edges of the tumor mass are poorly defined.

5.3.5 Enhanced Thermal Imaging

Enhanced thermal images were processed after acquisition using a temporal derivative method[52] that is sensitive to changes in temperature with time. Changes in temperature as a function of time were monitored both during and after LED illumination. These temperature changes were summed to create a single image, the temporal derivative image, that highlights the locations of blood and vascular structures (See Figure 5.6). The blood and vessels heat more than the surrounding tissue upon LED illumination as energy from the LED is strongly absorbed by blood in these regions. This

temporal derivative method highlights vascular structures by revealing regions of rapid temperature change during LED illumination. Tumors were evident in the enhanced thermal images on day 7 of the study (the first time mice were imaged after the initial injection of tumor cells) and tumor growth was monitored for the remainder of the study. Figure 5.6 shows a representative temporal derivative of the enhanced thermal images for one mouse on day 28 of the study. The green/yellow ring highlights the edges of the tumor mass. This ring is associated with a large temperature change upon LED illumination. LED illumination produced a temperature difference of approximately 0.4 °C between the blood rich corona and the surrounding tissue. The edges of the tumor mass are much sharper compared to standard thermal imaging (see Figure 5.5). The major and minor axes of the tumor were estimated by interactively selecting the length and width from each image using MATLAB. The average tumor volume (n=19) was derived from the enhanced thermal images. The tumor volume increases exponentially with time until the end of the study, similar to the results seen for the caliper measurements and for the IVIS imaging before day 22 (see Figure 5.2).

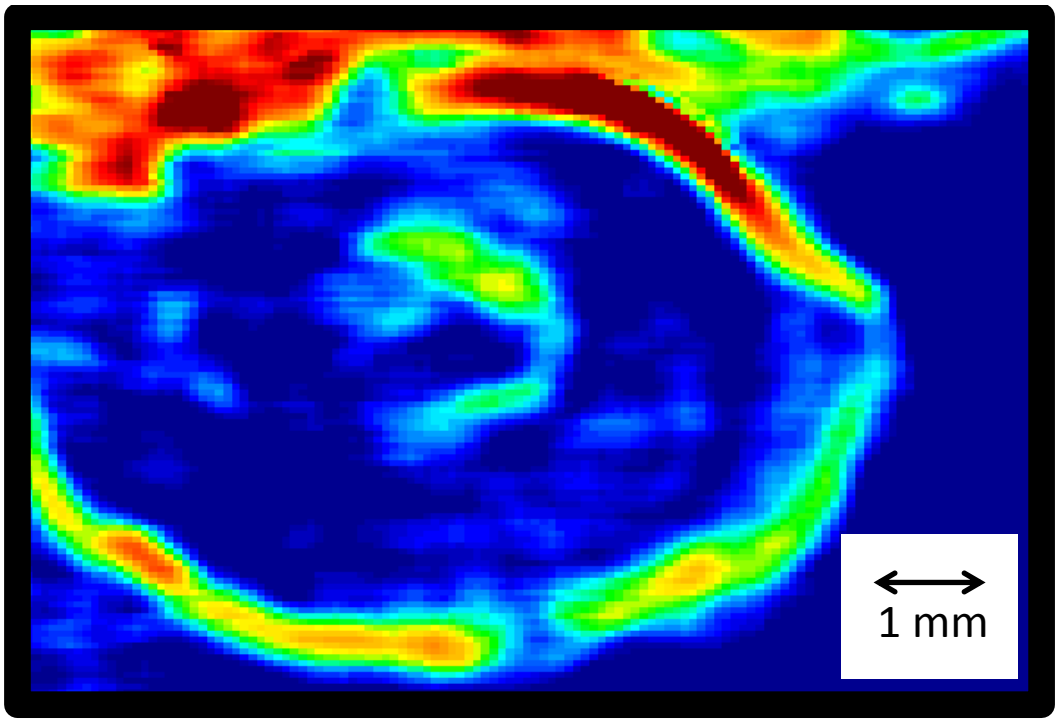

Figure 5.6: Representative temporal derivative of the enhanced thermal images of the tumor mass of one mouse on day 28 post-tumor implantation. Notice the yellow/green ring evident in the image that results from the selective heating of blood in this region. This ring delineates the edges of the tumor mass. The temperature difference between the blood rich corona and the surrounding tissue after LED illumination is approximately 0.4 °C.

5.3.6 Comparison of Caliper Measurements to Imaging Techniques

Caliper measurements physically determine the size of a tumor and accurately monitor tumor growth. We have compared the tumor growth measured using IVIS, enhanced thermal imaging and standard thermal imaging to caliper measurements to access the effectiveness of each of these techniques at monitoring tumor growth. Figure 7 depicts correlation plots for volumes based on physical caliper measurements and the various imaging techniques. In all cases the measurements exhibit a strong linear

correlation, meaning that all imaging techniques used are effective at monitoring tumor growth.

The tumor volumes measured with calipers compared to the volumes estimated by IVIS imaging from days 7-21 are strongly correlated (Figure 5.7; Adjusted R2=0.84). On the first day of the study, tumors were non-palpable and thus not measured using calipers and after day 21, necrotic areas and possible fluorescence signal loss affected the IVIS estimates. The linear fit to the correlation (slope=1.48) indicates that IVIS imaging measured tumor volumes that were approximately 50% larger than those measured using calipers.

Figure 5.7 also shows the correlation plot for tumor volumes measured with calipers compared to the volumes estimated by standard thermal imaging between days 7-30. The tumor volumes measured by calipers and the standard thermal images are strongly correlated (Adjusted R2=0.98). The linear fit to the correlation (slope=0.94) indicates that the volumes measured by both techniques are almost identical.

The correlation between tumor volumes measured with calipers and volumes estimated by enhanced thermal imaging (Figure 5.7) between days 7-30 is strong (Adjusted R2=0.99). The linear fit to the correlation (slope=1.52) indicates that the enhanced thermal imaging measured volumes that were approximately 50% larger than those estimated based on the caliper measurements throughout the study period.

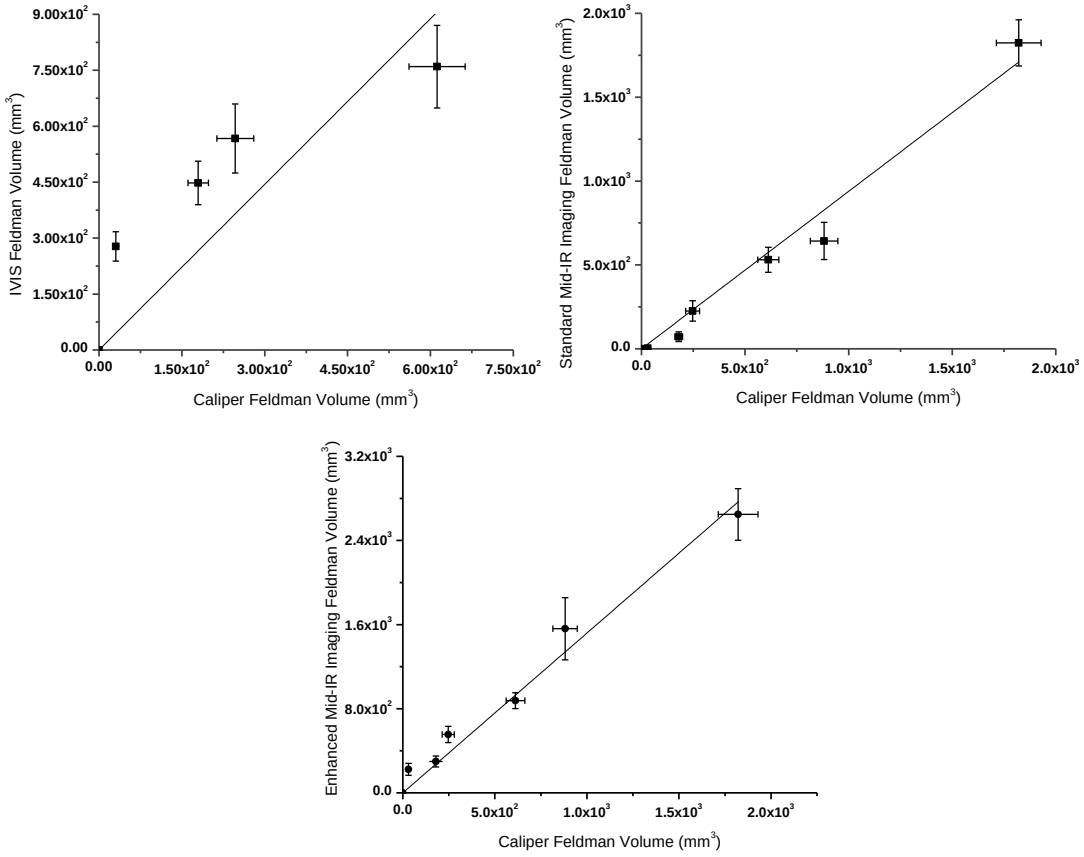

Figure 5.7: Comparison of tumor volumes measured using physical calipers with imaging techniques. a) Volumes estimated use caliper measurements and IVIS imaging are correlated (Adjusted R^2=0.84). The linear fit to the correlation (slope=1.48) indicates that IVIS imaging measures tumor volumes that are approximately 50% larger than those measured using calipers. b) Standard thermal imaging and physical caliper measurements have a nearly 1:1 (Slope=0.94) linear correlation (Adjusted R^2=0.98) indicating agreement of tumor volume estimates derived using these two techniques. c) Physical caliper and enhanced thermal imaging estimates of tumor volumes are strongly correlated (Adjusted R^2=0.99). Enhanced thermal imaging volume estimates are 52% larger (Slope=1.52) than the volumes derived from caliper measurements because enhanced thermal imaging detects the blood rich corona outside the tumor mass.

5.3.7 Comparison of Imaging Techniques

The IVIS fluorescent imaging is sensitive to the presence of cancer cells. As the number of cancer cells increases, the fluorescent signal increases and the estimated tumor

volume increases. IVIS imaging directly tracks the growth of the tumors over time. A correlation plot for the tumor volumes calculated using enhanced thermal imaging and IVIS imaging between days 7 and 21 is shown in Figure 8. The tumor volumes measured by the IVIS and enhanced thermal images are strongly correlated (Adjusted R2=0.96). This indicates that the enhanced thermal imaging also measures tumor growth. The linear fit to the correlation (slope = 1.00) indicates that the enhanced thermal imaging measured identical volumes to those estimated based on IVIS imaging.

Figure 5.8 shows a comparison of tumor volumes measured with standard thermal imaging compared to the volumes estimated by IVIS imaging as measured on days 7-21. The volumes are correlated (Adjusted R2=0.75) and the linear fit to the correlation (slope=0.47) indicates that the volumes measured by IVIS imaging are approximately two times larger than the volumes measured via standard thermal imaging.

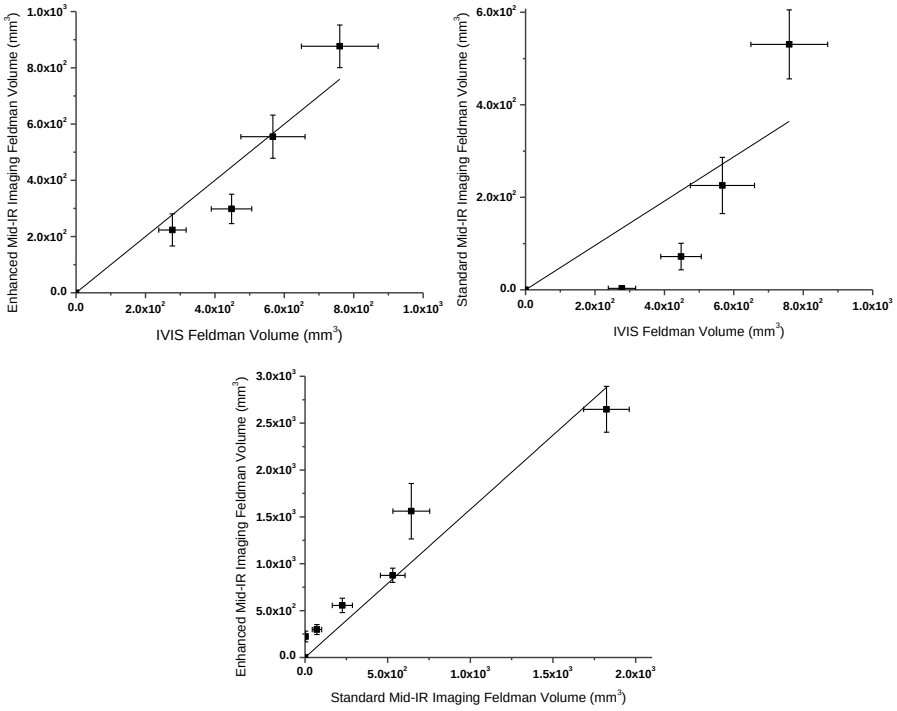

Figure 5.8: Comparison of tumor volumes measured using the three different imaging techniques used in this study. a) IVIS and enhanced thermal imaging measure almost identical tumor volumes (Adjusted R^2=0.96; slope=1.00) (b) Tumor volumes estimated from IVIS imaging are approximately two times larger than those estimated from standard thermal imaging (Adjusted R^2=0.75; slope=0.48). c) Volumes estimates based on enhanced thermal imaging and standard thermal imaging are strongly correlated (Adjusted R^2=0.95) with enhanced thermal imaging measuring a tumor volume approximately 58% percent larger (slope=1.58) than that estimated with standard thermal imaging. The larger volume results from detection the blood rich corona surrounding the tumor mass by the enhanced thermal imaging method.

Tumor volumes measured with enhanced thermal imaging and the volumes estimated by standard thermal imaging on days 7 – 30 are strongly correlated (Figure 5.8; Adjusted R2=0.95). The linear fit to the correlation (slope=1.58) indicates that the enhanced thermal imaging measured volumes that were approximately 58% larger than

those estimated based on standard thermal imaging. The larger volume is likely due to the fact that the enhanced thermal imaging is sensitive to vascular structures immediately outside the tumor mass, while the standard thermal images outline the tumor mass. Figure 5.9 shows an enhanced thermal image (contours) overlaid with a standard thermal image (color map) and clearly demonstrates that the bright corona seen in the enhanced thermal images is exterior to the tumor mass seen in the standard thermal image.

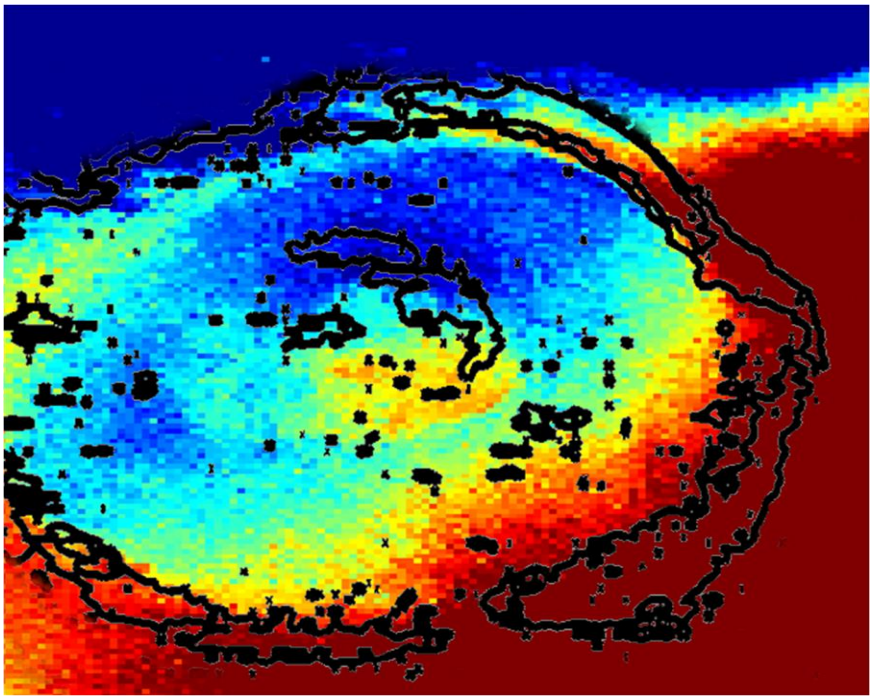

Figure 5.9: Representative standard thermal image (color map) shown with the temporal derivative of the enhanced thermal images (contours) of the same subject (from day 28 post-tumor implantation). Notice that the bright emission seen in the enhanced thermal image is exterior to the tumor mass seen in the standard thermal image.

5.3.8 Histology

Hematoxylin and Eosin staining (Figure 5.10) confirmed the presence of connective tissue containing fibroblasts but also tumor cells and vessels at the edge of the tumor mass (noted by the dotted line). The skin layer is also distinct in Figure 10. The FITC-dextran distribution highlights a higher blood content in the areas immediately surrounding the tumor mass (Figure 5.10). This area of increased vasculature is outside the tumor mass is seen as the bight halo in the enhanced thermal imaging.

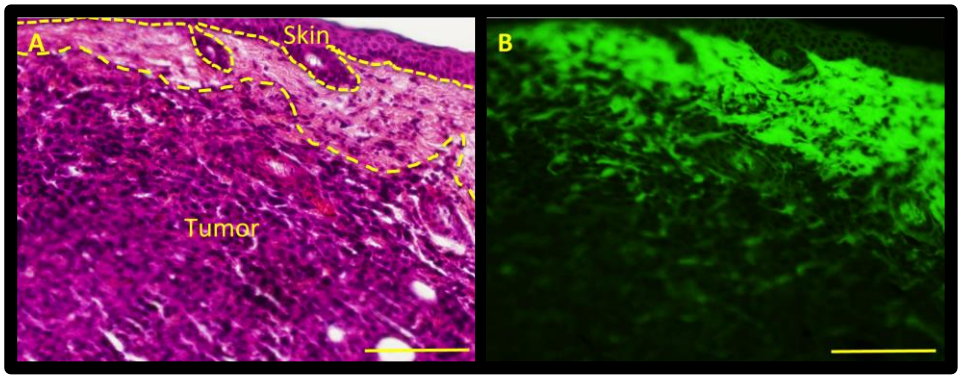

Figure 6.10: Edges of 4T1 tumors had increased blood distribution.
(A) Hematoxylin and Eosin staining confirm the presence at the edge of the tumor mass (noted by the dotted line) of connective tissue containing fibroblasts but also tumor cells. The skin layer is also distinct in this image. (B) FITC-dextran distribution in the 4T1 tumor mass indicating the presence of blood/blood vessels. Stronger fluorescent emission is seen in the region just exterior to the tumor mass (indicated by the bright green). Representative microphotographs, the scale bar represents 50 μm.

5.4 Conclusions

The results of this study indicate that enhanced thermal imaging allows for the detection and monitoring of mammary tumor masses and provides tumor volume estimates similar to physical caliper measurements and other imaging techniques. Further, enhanced thermal imaging highlights a blood rich vascular region around

tumors. This peri-tumoral zone is associated with early dissemination of tumor cells and is routinely targeted for surgical excision along with the tumor mass. Thus, enhanced thermal imaging may provide in real-time (i.e. during the surgery) a detailed map of the tumor margins improving patient outcomes.

CHAPTER 6: CONCLUSIONS

The overall goal of this study was to develop an enhanced mid-IR imaging modality for mapping vascular structures in real-time during surgical procedures. The study was divided into four parts to test different aspects of the project. The goal of the first study was to verify that selective heating of blood was possible using 405 and 530 nm LED sources. This selective heating would allow us to develop an enhanced mid-IR imaging technique that could yield high contrast images of vascular structures. We illuminated porcine tissue and blood with 405 and 530 nm LED sources and tracked the changes in temperature using a FLIR SC600 series mid-IR camera. The 530 nm wavelength LED at low powers, less than 500 mW/cm^2, heated blood more than other tissue types (fat, muscle and skin) which proved it to be a better light source for selectively heating blood compared to the 405 nm LED.

Expanding on the promising results using LEDs from our initial studies, we designed a set of *ex vivo* blood flow studies. The goal of these studies was to test ability of enhanced thermal imaging to map existing vascular networks in porcine heart tissue. These studies were successful in mapping subsurface vessels up to depths of 0.75 cm. In addition, image processing methods using a temporal and spatial derivative analysis were developed that further enhanced the ability of our system to map vasculature.

The results of the *ex vivo* flow studies demonstrated that our system could map vascular structures. However, the results only provided two-dimensional information

about the vessel locations and did not determine depth or size. We developed a series of heat transfer models for blood vessels embedded in muscle tissue using COMSOL Multiphysics. Based on the results of this modeling, we developed an algorithm to determine the depth and size of vessels from enhanced thermal images. We applied our algorithm to the previously obtained *ex vivo* blood flow studies as well as a set of gelatin tissue phantoms. We successfully determined depths and sizes for vessels embedded deeper than 2 mm. Further modeling will be required to improve the accuracy of the depth/size algorithm. Also the application of an iterative process may further enhance the predictive ability of this method.

We then applied out imaging technique to determine tumor margins with an *in vivo* study of breast cancer tumors in mice. Mice were injected with aggressive murine mammary cancer cells that mimic the later stages of breast cancer in humans. Our system was then used to monitor the tumor development for the next 30 days. Enhanced thermal images were acquired and processed using our temporal derivative method. The enhanced thermal images highlighted a vascular region just outside the tumor mass. This peri-tumoral zone is associated with early dissemination of tumor cells and is routinely targeted for surgical excision along with the tumor mass. Enhanced mid-IR imaging can be used to estimate tumor margins in real-time.

LEDs are an attractive alternative to laser sources due to their reliability and relative affordable price point. Also developments in the quality, performance and cost of mid-IR detectors have made thermal cameras more accessible for use in medicine. Our

enhanced mid-IR imaging system has the potential to be a low cost, reliable method for medical professionals to provide improved care for their patients.

MRI, CT and ultrasound are imaging techniques that are widely used in medicine today. Enhanced IR imaging offers a new low-cost imaging tool with similar spatial resolution as MRI and ultrasound. Enhanced IR imaging is faster and more cost effective than MRI and offers non-contact operation unlike ultrasound. While the spatial resolution of CT is greater, this technique uses ionizing radiation and this is not required with enhanced IR imaging. Enhanced thermal imaging has greater penetration depth (up to 0.75 cm in our *ex vivo* study) compared to OCT. Enhanced IR imaging is a promising imaging modality that is complimentary to other techniques used today.

Additional studies need to be completed to further test the ability of enhanced IR imaging to map tumor masses and to explore, in detail, the relationship between the vascular margins detected by our method and the cellular cancer margins mapped by histology. Ideally an additional *in vivo* study will be completed that, once again, looks at the development of breast cancer in murine models but with a much larger population. Also the addition of CT or MRI images of the tumors as they develop will allow a robust comparison with our method. Fluorescent imaging will also be included but the procedure will be to image a single subject at a time in the IVIS system. This will allow a significant increase in spatial resolution and possibly allow the direct tracking of tumor margins near the skin's surface from fluorescent signals. Ultimately, a study is humans will need to be completed.

In the future, the enhanced IR imaging technique could be improved in several ways. During this study we used a 530 nm LED source to heat blood. In the last year, new LED sources that emit closer to the peak absorption of hemoglobin (455 nm) have become available. This wavelength will likely more efficiently heat blood and blood vessels. Switching to one of these new LED sources will improve our imaging technique. In addition, recently FLIR systems has introduced new lenses that can further enhance our spatial resolution and eliminate the need for an external lens like the one used in the *in vivo* studies. To develop this technique for use by doctors, software that combines image collection and processing into one package must be developed.

REFERENCES

1. Lahiri BBB, Bagavathiappan S, Jayakumar T, Philip J. Medical applications of infrared thermography: A review. *Infrared Phys Technol*. 2012;55(4):221-235. doi:10.1016/j.infrared.2012.03.007.

2. Jan Mathias Gildemeister. Berkeley Bolometers: Why Bolometers? 2001. http://bolo.berkeley.edu/bolometers/introduction.html.

3. Barnes RB. Thermography of the Human Body: Infrared-radiant energy provides new concepts and instrumentation for medical diagnosis . *Sci* . 1963;140 (3569):870-877. doi:10.1126/science.140.3569.870 .

4. H. P-B, L.A. M-H, P.D. V-R, J.J. R-M, 2013 IEEE International Instrumentation and Measurement Technology Conference: Instrumentation and Measurement for Life I 2013. Thermal image processing for quantitative determination of temperature variations in plantar angiosomes. *Conf Rec IEEE Instrum Meas Technol Conf Conf Rec - IEEE Instrum Meas Technol Conf*. 2013:816-820.

5. Bagavathiappan S, Philip J, Jayakumar T, et al. Correlation between plantar foot temperature and diabetic neuropathy: a case study by using an infrared thermal imaging technique. *J diabetes Sci Technol*. 2010;4(6):1386-1392.

6. Armstrong DG, Lavery L a, Liswood PJ, Todd WF, Tredwell J a. Infrared dermal thermometry for the high-risk diabetic foot. *Phys Ther*. 1997;77(2):169-175; discussion 176-177.

7. Bharara M, Cobb JE, Claremont DJ. Thermography and thermometry in the assessment of diabetic neuropathic foot: a case for furthering the role of thermal techniques. *Int J Low Extrem Wounds*. 2006;5(4):250-260. doi:10.1177/1534734606293481.

8. Sun Z. Quality assessment and improvement in diabetes care-an issue now and for the future. *Diabetes Metab Res Rev*. 2010;26(6):446-447. doi:10.1002/dmrr.

9. Fushimi H, Inoue T, Nishikawa M, Matsuyama Y, Kitagawa J. A new index of autonomic neuropathy in diabetes mellitus: heat stimulated thermographic patterns. *Diabetes Res Clin Pract*. 1985;1(2):103-107.

10. Lavery L a., Higgins KR, Lanctot DR, et al. Preventing diabetic foot ulcer recurrence in high-risk patients: Use of temperature monitoring as a self-assessment tool. *Diabetes Care*. 2007;30(1):14-20. doi:10.2337/dc06-1600.

11. Benbow SJ, Chan AW, Bowsher DR, Williams G, Macfarlane IA. The prediction of diabetic neuropathic plantar foot ulceration by liquid-crystal contact thermography. *Diabetes Care*. 1994;17(8):835-839.

12. Schnell HM, Zaspel JG. Cooling extensive burns: sprayed coolants can improve initial cooling management - a thermography-based study. *Burns*. 2008;34(4):505-508. doi:10.1016/j.burns.2007.06.012.

13. Qi H, Diakides NA. Thermal infrared imaging in early breast cancer detection-a survey of recent research. 2003;2:1109-1112 Vol.2.

14. Ring F. Thermal imaging today and its relevance to diabetes. *J diabetes Sci Technol*. 2010;4(4):857-862. doi:10.1177/193229681000400414.

15. Bagavathiappan S, Saravanan T, Philip J, et al. Infrared thermal imaging for detection of peripheral vascular disorders. *J Med Phys*. 2009;34(1):43-47. doi:10.4103/0971-6203.48720.

16. Hosaki Y, Mitsunobu F, Ashida K, et al. Non-invasive study for peripheral circulation in patients with diabetes mellitus.

17. Simpson TL. Thermographic Tumor Detection Enhancemmel ~ lt Using Mi (: rowave Heating. *Medicine (Baltimore)*. 1978.

18. Deng Z-S, Liu J. Enhancement of thermal diagnostics on tumors underneath the skin by induced evaporation. *Conf Proc IEEE Eng Med Biol Soc*. 2005;7:7525-7528. doi:10.1109/IEMBS.2005.1616253.

19. Kosus N, Kosus A, Duran M, Simavli S, Turhan N. Comparison of standard mammography with digital mammography and digital infrared thermal imaging for breast cancer screening. *J Turkish Ger Gynecol Assoc*. 2010;11(3):152-157. doi:10.5152/jtgga.2010.24.

20. a AMKKK. Potential role of thermography in cancer management. 2010;2(6):300-312.

21. Wishart GC, Campisi M, Boswell M, et al. The accuracy of digital infrared imaging for breast cancer detection in women undergoing breast biopsy. *Eur J Surg Oncol*. 2010;36(6):535-540. doi:10.1016/j.ejso.2010.04.003.

22. Ng EYK, Kee EC. Integrative Computer-Aided Diagnostic With Breast Thermogram. *J Mech Med Biol*. 2007;07(01):1-10. doi:10.1142/S0219519407002091.

23. Yanmaz LE, Yanmaz LE, Okumus Z, Okumus Z, Dogan E, Dogan E. Instrumentation of Thermography and its Applications in Horses. *J Anim Vet Adv*. 2007;6(7):858-862.

24. Dunbar MR, Maccarthy KA, Journal S, Medicine W, Dec N, Maccarthy A. Use of Infrared Thermography to Detect Signs of Rabies Infection in Raccoons (Procyon lotor) Published by : American Association of Zoo Veterinarians Linked references are available on JSTOR for this article : You may need to log in to JSTOR to access t. 2015;37(4):518-523.

25. Wust P, Nadobny J, Szimtenings M, Stetter E, Gellermann J. Implications of clinical RF hyperthermia on protection limits in the RF range. *Health Phys*. 2007;92(6):565-573.

26. Vogel A, Venugopalan V. Mechanisms of pulsed laser ablation of biological tissues. *Chem Rev*. 2003;103(2):577-644. doi:10.1021/cr010379n.

27. Poetke M, Berlien H-P. Laser treatment in hemangiomas and vascular malformations. *Med Laser Appl*. 2005;20(2):95-102. doi:10.1016/j.mla.2005.03.008.

28. Amador Kane S. *Introduction to Physics in Modern Medicine*. 2nd ed. CRC Press; 2009.

29. Kalapurayil M. What is an MRI? How does an MRI work? 2009.

30. ASSH. *Am Soc Surg Hand*. 2006. http://www.assh.org/Public/HandConditions/Pages/VascularDisorders.aspx.

31. Nordqvist C. What is a CT scan? What is a CAT Scan? 2009. http://www.medicalnewstoday.com/articles/153201.php.

32. Nordqvist C. What is an Ultrasound? 2012. http://www.medicalnewstoday.com/articles/245491.php.

33. Nelson JS, Kelly KM, Zhao Y, Chen Z. Imaging blood flow in human port-wine stain in situ and in real time using optical Doppler tomography. *Arch Dermatol*. 2001;137(6):741-744.

34. Hu S, Wang L V. Photoacoustic imaging and characterization of the microvasculature. *J Biomed Opt*. 2012;15(1):011101. doi:10.1117/1.3281673.

35. Laufer J, Johnson P, Zhang E, et al. In vivo preclinical photoacoustic imaging of tumor vasculature development and therapy. *J Biomed Opt*. 2012;17(5):056016. doi:10.1117/1.JBO.17.5.056016.

36. Kalapurayil M. What is an MRI? How does an MRI work? 2009. http://www.medicalnewstoday.com/articles/146309.php.

37. Probst J, Hillmann D, Lankenau E, et al. Optical coherence tomography with online visualization of more than seven rendered volumes per second. *J Biomed Opt*. 2010;15(2):026014. doi:10.1117/1.3314898.

38. Rodrigues DB, Pereira PJS, Limão-Vieira P, Stauffer PR, Maccarini PF. Study of the one dimensional and transient bioheat transfer equation: Multi-layer solution development and applications. *Int J Heat Mass Transf*. 2013;62(1):153-162. doi:10.1016/j.ijheatmasstransfer.2012.11.082.

39. Keangin P, Wessapan T, Rattanadecho P. Analysis of heat transfer in deformed liver cancer modeling treated using a microwave coaxial antenna. *Appl Therm Eng*. 2011;31(16):3243-3254. doi:10.1016/j.applthermaleng.2011.06.005.

40. Marqa M-F, Colin P, Nevoux P, Mordon SR, Betrouni N. Focal laser ablation of prostate cancer: numerical simulation of temperature and damage distribution. *Biomed Eng Online*. 2011;10(1):45. doi:10.1186/1475-925X-10-45.

41. Loureiro FS, Mansur WJ, Wrobel LC, Silva JE a. The Explicit Green's Approach with stability enhancement for solving the bioheat transfer equation. *Int J Heat Mass Transf*. 2014;76:393-404. doi:10.1016/j.ijheatmasstransfer.2014.04.064.

42. Deng Z-S, Liu J. Analytical study on bioheat transfer problems with spatial or transient heating on skin surface or inside biological bodies. *J Biomech Eng*. 2002;124(6):638-649. doi:10.1115/1.1516810.

43. Opieliński KJ, Pruchnicki P, Gudra T, et al. Imaging Results of Multi-modal Ultrasound Computerized Tomography System Designed for Breast Diagnosis. *Comput Med Imaging Graph*. 2015. doi:10.1016/j.compmedimag.2015.02.004.

44. Wang L, Hu S. Photoacoustic Tomography: in Vivo Imaging Fro Organelles To Organs. *Science (80-).* 2012;335(6075):1458-1462. doi:10.1126/science.1216210.Photoacoustic.

45. King RL, Liu Y, Maruvada S, Herman BA, Wear KA, Harris GR. Development and characterization of a tissue-mimicking material for high-intensity focused

ultrasound. *IEEE Trans Ultrason Ferroelectr Freq Control*. 2011;58(7):1397-1405. doi:10.1109/TUFFC.2011.1959.

46. American Cancer Society, Inc. Atlanta G. Cancer Facts & Figures. 2015.

47. Giuliano AE, Hunt KK, Ballman K V, et al. Axillary dissection vs no axillary dissection in women with invasive breast cancer and sentinel node metastasis: a randomized clinical trial. *JAMA*. 2011;305(6):569-575. doi:10.1001/jama.2011.90.

48. Song JB, Vemana G, Mobley JM, Bhayani SB. The second "time-out": a surgical safety checklist for lengthy robotic surgeries. *Patient Saf Surg*. 2013;7(1):19. doi:10.1186/1754-9493-7-19.

49. Herranz M, Ruibal A. Optical imaging in breast cancer diagnosis: The next evolution. *J Oncol*. 2012;2012. doi:10.1155/2012/863747.

50. Siegel JS. The breast cancer landscape. *Nature*. 2012;486(7403):2-3. doi:10.1038/486328a.

51. Roggan A, Friebel M, Do K, et al. Optical properties of circulating human blood in wavelength range 400-2500 nm. 1999;4(1):36-46.

52. Case JR, Young MA, Keanini RG, Trammell SR. Using LED sources to selectively heat blood for enhanced mid-IR imaging of vascular structures. *OSA Tech Dig*. 2014;Biomedical.

53. Perkin Elmer. Living lmage ® Software User's Guide. 2006;(February).

54. Jewell AN, Swamydas M, Castillo CI, et al. The endothelin axis stimulates the expression of pro-inflammatory cytokines and pro-migratory molecules in breast cancer. *Cancer Invest*. 2010;28(19):932-943. doi:10.3109/07357907.2010.496757.

55. Feldman JP, Goldwasser R. Quantitative Methods Inquires: A mathematical model for tumor volume evaluation. *Methods*. 4(4):455-462.

56. Shackney SE. *Tumor Growth, Cell Cycle Kinetics and Cancer Treatment*. McGraw Hill, New York; 1993.

APPENDIX A: TISSUE PHANTOM INFORMATION

Table A.1: Tissue Phantom Thermal Properties[45]

Tissue Phantom Thermal Properties	
Thermal Conductivity ($W \cdot m^{-1} \cdot °C^{-1}$)	0.56-0.65
Thermal Diffusivity ($mm^2 \cdot s^{-1}$)	0.11-0.13

Recipe for tissue 200 mL of tissue phantom[45]:

1. Mix 0.2 g of potassium sorbate with 0.8 g of calcium chloride and 40 mL of water, stirring continuously.
2. Mix 3 g of gellan gum with 160 mL of water, stirring continuously.
3. Heat gellan gum mixture to a simmer on a hot plate while heating calcium chloride/potassium sorbate mixture to 80ºC.
4. Once the gellan gum begins to simmer turn off the hot plate and mix in the calcium chloride mixture, stirring continuously while the total mixture cools on the hot plate.
5. Once the final mixture reaches approximately 76 ºC transfer the contents to your dish and let sit for 1-2 hours.

APPENDIX B: PATENTS AND PUBLICATIONS

Jason R. Case and Susan R. Trammell "Thermal Detection and Mapping of Tumors," U.S. Patent PCT/US15/017035 filed Feb. 23, 2015.

Jason R. Case, Madison A. Young, Susan R. Trammell, "Heat Transfer Models of Heated Blood Vessels Embedded in Muscle to Aid in the Development of an Algorithm to Determine the Depth and Radius of Vascular Structures Imaged Using Enhanced Mid-IR Imaging." 2015 J. Med. Im. (in preparation)

Jason R. Case, Madison A. Young, Michelle M. Phelps, Rachel S. Helms, D. Dreau, Susan R. Trammell, "Non-Invasive Mid-IR Detection of Breast Cancer Tumor Development *In Vivo*" 2015, J. Biomed. Opt. (submitted).

Jason R. Case, Madison A. Young, Didier Dreau, Susan R. Trammell, "Non-invasive thermal IR detection of breast tumor development in vivo" SPIE Medical Imaging Feb 23, 2015; Paper 9412-176 (Awarded Cum Laude)

J. Case, M. Young, R. Keanini, and S. Trammell,"Using LED sources to selectively heat blood for enhanced mid-IR imaging of vascular structures," in Biomedical Optics 2014, OSA Technical Digest (online) (Optical Society of America, 2014), paper BS5A.1.

Jason R. Case ; Susan R. Trammell ; Madison A. Young ; Uriah Israel ; Michael X. Crown; "Heat as a contrast agent to enhance thermal imaging of blood vessels," Proc. SPIE 8565, Photonic Therapeutics and Diagnostics IX, 85654H (March 8, 2013); doi:10.1117/12.2004790.

Jason R. Case, "Using LED Sources to Create Contrast Agents For Mid-Infrared Imaging of Blood Vessels," M.S. Thesis, Dept. of Physics and Optical Sci., UNC Charlotte, Charlotte, NC, 2012.